Research

Check for updates

Author for correspondence:
Jacopo Ciambella
e-mail: jacopo.ciambella@uniroma1.it

An Ogden-like formulation incorporating phase-field fracture in elastomers: from brittle to pseudo-ductile failures

Jacopo Ciambella[1], Giovanni Lancioni[3] and Nico Stortini[2]

[1]Department of Structural and Geotechnical Engineering, Sapienza University of Rome, Rome, Italy
[2]Department of Civil and Building Engineering and Architecture, Polytechnic University of Marche, Ancona, Italy
[3]Department of Mechanics and Aeronautics, Sapienza University of Rome, Rome, Italy

JC, 0000-0002-7498-5821

Over the past 50 years the Ogden model has been widely used in material modelling owing to its ability to match accurately the experimental data on elastomers at large strain, as well as its mathematical properties, such as polyconvexity. In this paper, these characteristics are exploited to formulate a finite-strain model that incorporates, through the phase-field approach recently proposed by Wu (Wu 2017 *J. Mech. Phys. Solids* **103**, 72–99) for small strains, a cohesive damage mechanism which leads to the progressive degradation of the material stiffness and to failure under tension. By properly tailoring the constitutive parameters, the model is capable of encompassing a wide range of effects, from brittle to pseudo-ductile failure modes. A plane stress problem is formulated to test the model against experiments on double-network elastomers, which display a pseudo-ductile damage behaviour at large strain, and on conventional rubber compounds with brittle failure. The results show that the proposed model is applicable to fracture coalescence and propagation in a wide range of materials.

This article is part of the theme issue 'The Ogden model of rubber mechanics: Fifty years of impact on nonlinear elasticity'.

1. Introduction

Over the past 50 years the phenomenological hyperelastic model proposed by Ogden for compressibile [1] and incompressibile [2] elastomers has been successfully adopted for a variety of materials including rubber [3–6], nematic elastomers [7,8], foams [9,10], biological tissues [11–13] and even carbon nanotubes [14]. The main feature of the Ogden model is that it postulates a form of the strain energy density in terms of the principal stretches rather than the classical invariants of strain, making the closed-form expression of the tangent moduli easily calculable [3] and the model easily implementable in finite-element algorithms. In addition, the model has the property of polyconvexity.

The strain energy density is written as the sum of three separate functions of the principal stretches λ_1, λ_2 and λ_3:

$$\phi(\lambda_1, \lambda_2, \lambda_3) = \sum_{a=1}^{3} \tilde{\phi}(\lambda_a), \quad \text{with} \quad \tilde{\phi}(\lambda_a) = \sum_{n=1}^{N} \frac{\mu_n}{\alpha_n}(\lambda_a^{\alpha_n} - 1), \tag{1.1}$$

making it adherent to the so-called Valanis–Landel split [15]. Each term $\tilde{\phi}(\lambda_a)$ represents the elastic energy of a nonlinear spring undergoing a stretch λ_a; the corresponding stiffness $\mu_n \alpha_n$ can be tailored to describe all aspects of the rubber elastic response, from the initial softening for moderate strains to the stress-hardening at large strains. For most quasi-static experiments on rubber, the three terms in the series give an excellent correlation with stress–strain data [16].

The remarkable properties of the Ogden model are exploited in this paper to formulate a theory for the cohesive failure of elastomeric materials at large strain. The hyperelastic energy (1.1) is used in conjunction with a phase-field variable to describe the mechanisms which lead to the softening behaviour and to the progressive degradation of the material stiffness. The degradation function, weighing the elastic energy reduction due to damage, is appropriately chosen to describe brittle and quasi-brittle failure modes. In defining the model, we have followed the phase-field approach introduced in [18], where the fracture problem was formulated as a free-discontinuity minimum problem. The variational formulation of fracture was infact approximated in [19] by a regularized problem that operates on a functional defined on continuous fields, with the fracture replaced by the so-called *phase-field* variable. Acting like a damage variable, the phase-field assumes values between 0 and 1, with 0 for sound material and 1 for fractured material, and its evolution describes the coalescence and propagation of cracks [20–22]. As the phase-field increases, the stiffness of the material reduces, vanishing when the damage variable reaches 1. A non-local term, proportional to the gradient of the phase-field, is incorporated into the internal energy functional and plays the role of a localization limiter by penalizing abrupt damage variations [23]. The gradient contribution automatically introduces an internal length, which in the present formulation is a constitutive parameter to be calibrated through experimental data [24], and it makes the model size-dependent. The smoothness properties of such a phase-field approach allow for straightforward finite-element implementation, and no remeshing or *ad hoc* numerical strategies need to be used, making the solution of the numerical problem robust and independent of the mesh used in the finite-element simulations.

Over the years, many contributions in the literature have dealt with phase-field formulations for brittle materials, but a model incorporating brittle and cohesive failures at large strain is still missing. A first approach to defining phase-field fracture within the framework of finite elasticity was proposed in [25]. Subsequent works have dealt with rate-independent fracture [23] and with the inclusion of viscous effects [26]. A multiplicative splitting of the stretch into tensile and compressive parts was proposed in [27] to describe fracture mechanisms induced by tensile stress states. Cavitation processes in elastomers, with voids coalescing and developing into fractures, were reproduced in [28] by using a specific nonlinear polyconvex strain energy density. A phase-field model for the description of cavitation was also proposed in [29] and improved in [30], according to the experimental evidence of Poulain *et al.* [31,32]. A bottom-up multi-scale approach was followed in [33]. It was assumed that the internal energy on the micro-scale is composed of

an entropic contribution due to the polymer chains' configurational entropy and an energetic contribution due to bond deformation, such that the latter contribution drives crack nucleation, initiation and propagation. Then, bridging the microscopic assumptions to the macro-scale, a continuum model was obtained where fracture was approximated by a phase-field. A phase-field model was also proposed in [34] based on the micro-mechanics of polydisperse elastomer networks, that is, distributions of polymeric chains with different lengths.

Although elastomers are capable of sustaining large deformations, most of the time their failure is brittle, and this peculiarity potentially reduces the range of applications. To overcome this limitation, new elastomeric compounds are being developed that have increased ductility and durability, usually achieved by tailoring the material microstructure to have a progressive damage process which only gradually leads to fracture. These failure modes are usually observed in highly filled elastomers, in which the mechanism of cohesive failure is activated at the filler–matrix interface [35], or in multiple-network elastomers, where the presence of the additional filler network leads to a strong localized softening, due to rupture of covalent bonds and coalescence of defects [36,37].

A versatile phase-field model should be able to describe the different failure modes seen in the experiments, from the brittle failure of conventional elastomers to the pseudo-ductile failure of double-network elastomeric compounds, without using any information on the material microstructure in the spirit of the Ogden's phenomenological approach. With this intent, we propose a novel phase-field model in which the elastic energy is defined through an Ogden-like strain energy function and the energetic functionals of fracture are of the type introduced in [17]. In this latter paper, brittle and quasi-brittle failures were captured within the context of infinitesimal elasticity, with a model able to reproduce the softening laws frequently adopted in the literature for quasi-brittle solids, e.g. linear, exponential or hyperbolic. Thus the popular phase-field models for brittle fracture, e.g. those in [21,22], were recovered as particular examples.

Extension of the formulation in [17] would allow description of all the relevant failure modes seen in elastomers by properly tailoring the relevant constitutive parameters of the fracture energetic functionals. However, the mechanical interpretation of these coefficients has to be carefully assessed in the context of finite elasticity, since their role differs from that observed at small strains. For this reason, a fundamental task of the present work is to comprehend the influence of the constitutive parameters on the damage evolution modes in order to gain a clear picture of the predictive potential of the model. Analytical and numerical estimates were obtained to correlate the shape of the damage energy and degradation functions with the predicted damage modes. To focus on this, no further modelling ingredients, such as thermal or viscous contributions, were included in the formulation, by assuming that crack propagation is rate-independent. Indeed, viscous effects in fracture evolution are negligible for low rates of tearing, as shown in [38]. Furthermore, we consider only fracture processes induced by tensile stress states; yet crack opening under compressive loadings can be avoided by introducing the same elastic energy splitting used in [39–41]. The optimal constitutive parameters of the model were calibrated by studying the one-dimensional problem of a bar under traction, which allowed us to solve the problem in semi-analytical form.

The structure of the paper is the following. Section 2 is devoted to the formulation of the three-dimensional model in a consistent thermodynamic framework. It addresses the theoretical aspects of the proposed phase-field theory. Section 3 focuses on the calibration of the model parameters by solving the one-dimensional problem of a bar under traction. The numerical solutions of some prototypical examples are presented and discussed in §4, including a thorough comparison of the model prediction with the experimental data in [36] and in [56]. Concluding remarks are given in §5.

2. Model formulation

In this section, we aim to formulate the nonlinear elastic model with damage in a three-dimensional plane stress setting, before carrying out a sensitivity analysis in §3 by considering

the response of a bar under traction. The approach taken to equilibrium is based on a unilateral minimality principle under the condition of irreversibility of the damage field. The same approach has been widely adopted in studying plasticity [25,42,43], plasticity with damage [44,45] and cohesive damage [17,46].

Throughout the paper, we will assume that all fields are sufficiently smooth so that all the calculations can be performed. For a precise definition of the functional spaces needed the reader is referred to [47].

A note on the notation. In the following, lower-case bold letters will be used for points or vectors, and capital bold letters for tensors. The inner product between two vectors or two tensors of the same order will be indicated by a dot, e.g. $\mathbf{a} \cdot \mathbf{b} = \sum_i a_i b_i$ or $\mathbf{A} \cdot \mathbf{B} = \sum_{i,j} A_{ij} B_{ij}$. An overdot will indicate the material time derivative, whereas a prime will denote the derivative with respect to the independent variable, e.g. the position x or the variable d.

(a) State variables

We identify a body with a region Ω_0 of the three-dimensional Euclidean space $\mathcal{E}$ that it occupies at some time instant $t = 0$, which we refer to as the *reference configuration*. The external boundary $\partial \Omega_0$ is divided into a subset $\partial \Omega_0^u$ in which displacement is applied and a complementary boundary $\partial \Omega_0^t$ in which surface forces are present. The deformation of the body is the bijective orientation-preserving map $p : \Omega_0 \times [0, t] \to \mathcal{E}$ which assigns to each point $\mathbf{x} \in \Omega_0$ a point $\mathbf{y} = p(\mathbf{x}, t)$ in the deformed configuration; accordingly we set $\Omega_t = p(\Omega_0, t)$ as the deformed configuration of the body.

At each material point $\mathbf{x}$, the state of the continuum is identified by the displacement field $\mathbf{u}(\mathbf{x}, t)$ and by an additional scalar field $d(\mathbf{x}, t)$ that represents the *damage variable*, such that $d = 0$ for the virgin material and $d = 1$ for the fully damaged one; in this formulation, d is a Lagrangian parameter defined on the reference configuration Ω_0. We further denote by $\mathcal{U}$ the space of kinematically admissible displacement fields,

$$\mathbf{u}(\mathbf{x}, t) \in \mathcal{U} := \{\mathbf{u} : \mathbf{u}(\mathbf{x}, t) = \mathbf{u}^* \; \forall \mathbf{x} \in \partial \Omega_0^u\},$$

and denote by $\mathcal{D}$ the set of the admissible damage fields,

$$d(\mathbf{x}, t) \in \mathcal{D} := \{d : d(\mathbf{x}, t) \in [0, 1]\}.$$

We denote the deformation gradient by $\mathbf{F} = \mathbf{I} + \nabla \mathbf{u}$, where $\nabla = \partial/\partial \mathbf{x}$ is the gradient operator defined with respect to the reference coordinates $\mathbf{x}$ and $\mathbf{I}$ is the unit tensor.

The variations $\tilde{\mathbf{u}}$ and $\tilde{d}$ will be used in the application of the minimality principle to derive the governing equations of the problem. These have to satisfy homogeneous boundary conditions, and as such belong to the following sets:

$$\tilde{\mathbf{u}}(\mathbf{x}, t) \in \widetilde{\mathcal{U}} := \{\tilde{\mathbf{u}}(\mathbf{x}, t) = \mathbf{0} \; \forall \mathbf{x} \in \partial \Omega_0^u\} \tag{2.1}$$

and

$$\tilde{d}(\mathbf{x}, t) \in \widetilde{\mathcal{D}} := \{\tilde{d} : \tilde{d}(\mathbf{x}, t) \geq 0 \text{ for almost all } \mathbf{x} \in \Omega_0\}, \tag{2.2}$$

the latter being the convex cone of positive damage rate. As will be apparent in the following sections, in the present formulation the damage variable can only increase (no-healing).

For the sake of conciseness, the explicit dependence on the position $\mathbf{x}$ and time t will be omitted from all variables except when needed.

(b) Energy functional

The behaviour of the continuum is characterized at each material point $\mathbf{x}$ and at each time instant t by two state variables $\{\mathbf{u}, d\}$ in $\mathcal{U} \times \mathcal{D}$ and by a state function φ, which gives the energy density at each material point; φ depends on the local strain $\mathbf{F}(\mathbf{x})$, the value of the damage variable $d(\mathbf{x})$

and the local value of the damage gradient $\nabla d(\mathbf{x})$, with the functional form

$$\varphi(\nabla \mathbf{u}, d, \nabla d) = \overbrace{\psi(\mathbf{I} + \nabla \mathbf{u}, d)}^{\text{elastic energy}} + \overbrace{\frac{G_c}{c\,b}\eta(d) + b\frac{G_c}{c}|\nabla d|^2}^{\text{fracture energy}}, \qquad (2.3)$$

which is composed of the following three terms:

— $\psi(\mathbf{I} + \nabla \mathbf{u}, d)$, the *elastic energy* at the damage state d;
— $G_c\eta(d)/(cb)$, which can be interpreted as the *fracture energy* during a homogeneous damage process with $\nabla d = 0$;
— $bG_c|\nabla d|^2/c$, the *nonlocal* term which limits the possibility of damage localization without any energetic cost (see for instance [22]); this term introduces an intrinsic length scale which controls the size of the damage localization zone.

The second and third terms in equation (2.3) constitute the *non-local fracture energy density*, in which the constitutive parameter G_c is the *critical elastic energy release rate*, b represents an internal length that regularizes the sharp crack and $c := 4\int_0^1 \sqrt{\eta(d)}\,\mathrm{d}d$ is a scaling parameter [40]. The relationship between the state function φ and the free-energy density of such a material is discussed in remark 2.2 of §2c.

We further assume that the elastic strain energy density ψ can be multiplicatively decomposed as

$$\psi(\mathbf{I} + \nabla \mathbf{u}, d) = \omega(d)\,\psi_0(\mathbf{I} + \nabla \mathbf{u}), \qquad (2.4)$$

in which $\psi_0(\mathbf{I} + \nabla \mathbf{u})$ is the elastic energy density of the neat material and $\omega(d)$ is a monotonically decreasing energetic *degradation function* describing the degradation of the stored energy with evolving damage. The bulk strain energy density ψ_0 is a continuous isotropic function such that $\psi_0(\cdot)$ is frame indifferent. Such a requirement implies that for any given deformation $\mathbf{F}$, one has $\psi_0(\mathbf{Q}^\mathsf{T}\mathbf{F}\mathbf{Q}) = \psi_0(\mathbf{F})$ (isotropic response) and $\psi_0(\mathbf{Q}^\mathsf{T}\mathbf{F}) = \psi_0(\mathbf{F})$ (frame indifference) for every rotation matrix $\mathbf{Q}$.

The energetic degradation function $\omega(d)$ plays an important role in determining the properties of the material, and, consistent with the experimental observation, we assume that

$$\omega'(d) < 0 \quad \text{and} \quad \omega(0) = 1, \quad \omega(1) = 0, \quad \omega'(1) = 0, \qquad (2.5)$$

where the latter constraint ensures that the energetic fracture converges to a finite value if the damage converges to the fully broken state (see [23]).[1] Motivated by the analysis presented in [17], the following form of the degradation function ω is considered:

$$\omega(d) := \frac{(1-d)^2}{(1-d)^2 + a_1 d(1 + a_2\,d + a_2 a_3 d^2)}, \qquad (2.6)$$

where a_1, a_2 and a_3 are constitutive parameters, whose calibration allows the description of different fracture modes, from brittle to pseudo-ductile, as shown in §3 with uniaxial numerical tests. The chosen form of ω heavily affects the softening behaviour once the crack is initiated.

The dissipated energy density plays a significant role in the evolution of the damage as well. We assume $\eta(d)$ to have the quadratic expression

$$\eta(d) = 2d - d^2, \qquad (2.7)$$

such that $\eta(0) = 0$ and $\eta(1) = 1$. With this assumption, the scaling parameter c becomes $c = 4\int_0^1 \sqrt{2d - d^2}\,\mathrm{d}d = \pi$. We point out that different choices can be made for the function $\eta(d)$; the interested reader is referred to [17] for a full account of the different possibilities.

---

[1]In the numerical examples carried out in §4, a small positive value of the degradation function is assumed when the material is fully broken. This is a standard technique to guarantee that the numerical problem remains well-posed for a broken specimen.

With the definition (2.3) of the state variable φ, we are in a position to define the total energy stored in the material during the deformation process. For each admissible pair $(\mathbf{u}, d) \in \mathscr{U} \times \mathscr{D}$, the total energy of the continuum is

$$\mathcal{I}(\mathbf{u}, d) = \int_{\Omega_0} \varphi(\nabla \mathbf{u}, d, \nabla d) - \int_{\Omega_0} \mathbf{b}_0 \cdot \mathbf{u} - \int_{\partial \Omega_0^t} \mathbf{t}_0 \cdot \mathbf{u}, \tag{2.8}$$

$\mathbf{b}_0$ and $\mathbf{t}_0$ being the forces per unit reference volume and area, respectively, the latter applied on the part of the boundary $\partial \Omega_0^t$. These latter terms represent (negative) the work expended by the external forces.

(i) Ogden-like strain energy

Considering the incompressibility of rubbery polymers, the elastic strain energy density that appears in (2.4) can be decomposed into isochoric and volumetric parts,

$$\psi_0(\mathbf{F}) = \psi_0^{\text{iso}}(\bar{\mathbf{F}}) + U(J),$$

where $\bar{\mathbf{F}} = J^{-1/3} \mathbf{F}$ and $J = \det(\mathbf{F})$. In this work, however, we only consider *plane stress* cases, meaning that the unknown pressure field associated with the incompressibility constraint $J = 1$ can always be determined via substitution in the out-of-plane deformation [48].

In the spirit of Ogden's phenomenological model, we formulate the strain energy density in terms of the principal stretches λ_1, λ_2 and λ_3 of $\mathbf{F}$. In doing so, we set $J = 1$ and $\lambda_3 = (\lambda_1 \lambda_2)^{-1}$ and follow [2] in assuming the following form[2] of ψ_0:

$$\psi_0 = \phi(\lambda_1, \lambda_2) = \sum_{n=1}^{N} \frac{\mu_n}{\alpha_n} (\lambda_1^{\alpha_n} + \lambda_2^{\alpha_n} + (\lambda_1 \lambda_2)^{-\alpha_n} - 3), \tag{2.9}$$

where ϕ is the elastic energy density expressed in terms of the two independent principal stretches λ_1 and λ_2, from which we have omitted the dependence on $\mathbf{F}$. We note that the formulation (2.9) satisfies both frame invariance and isotropy.

In equation (2.9), N is a positive constant, usually $N = 3$ for most experiments on rubber, and μ_n and α_n are material constants such that $\mu_n \alpha_n > 0$ and $\sum_{n=1}^{N} \mu_n \alpha_n = 2\mu$, μ being the shear modulus of the material.

As a reference for the calculations in the next sections, we compute the Piola stress tensor, that is, the dual quantity to $\nabla \tilde{\mathbf{u}}$ in this energetic formulation (see equation (2.13)). With the definition of Ogden's energy (2.9) and the hypothesis that $\lambda_3 = (\lambda_1 \lambda_2)^{-1}$, we obtain

$$\mathbf{S} = \frac{\partial \psi}{\partial \mathbf{F}} = \omega \sum_{i=1}^{2} \phi_{,i} \, \mathbf{n}_i \otimes \mathbf{N}_i, \quad \|\mathbf{n}_i\| = \|\mathbf{N}_i\| = 1, \tag{2.10}$$

where

$$\phi_{,1} := \frac{\partial \phi}{\partial \lambda_1} = \sum_{n=1}^{N} \mu_n (\lambda_1^{\alpha_n - 1} - (\lambda_1 \lambda_2)^{-\alpha_n - 1} \lambda_2)$$

and

$$\phi_{,2} := \frac{\partial \phi}{\partial \lambda_2} = \sum_{n=1}^{N} \mu_n (\lambda_2^{\alpha_n - 1} - (\lambda_1 \lambda_2)^{-\alpha_n - 1} \lambda_1)$$

are the derivatives of the strain energy density $\phi(\lambda_1, \lambda_2)$ with respect to the principal stretches obtained by using the relationships reported in [3]. The directions $\{\mathbf{n}_1, \mathbf{n}_2, \mathbf{e}_3\}$ are the eigenvectors of the left stretch tensor $\mathbf{V}$ ($\mathbf{V}^2 = \mathbf{F}\mathbf{F}^{\text{T}}$), and $\{\mathbf{N}_1, \mathbf{N}_2, \mathbf{e}_3\}$ are the eigenvectors of the right stretch tensor $\mathbf{U}$ ($\mathbf{U}^2 = \mathbf{F}^{\text{T}}\mathbf{F}$), whereas $\mathbf{e}_3$ is assumed to be the direction of plane stress perpendicular either to $\{\mathbf{n}_1, \mathbf{n}_2\}$ or to $\{\mathbf{N}_1, \mathbf{N}_2\}$.

---

[2]This assumption is equivalent to assuming that the elastomer deforms in a perfectly incompressible way even after damage has occurred. This simplification can in fact be removed by coupling compressibility and damage growth, but we do not address this in the present work.

(c) Governing equations

The derivation of the governing equations of the problem, including the damage evolution, is carried out following the classical variational approach to fracture mechanics (see for instance [22] or [24]), which consists of:

1. the *damage irreversibility* condition, $\dot{d}(\mathbf{x}, t) \geq 0$ and $d(\mathbf{x}, 0) = 0$;
2. a *stability criterion*, which is in fact a necessary condition for the unilateral minimality condition on the functional (2.8);
3. the *energy balance principle*, which states that the total energy at time t is equal to the work of the external forces up to time t.

A posteriori it is shown that under the imposed constitutive assumptions, the *dissipation inequality*, that is, the second principle of thermodynamics, is also satisfied.

(i) Stability condition

Starting from an undamaged state at $t = 0$, we say that the process evolves through stable equilibrium configurations if and only if at each time instant the system attains a local minimum of the total energy (2.8). This leads us to introduce the following *stability condition*:

$$
\text{For each } t > 0, \{\mathbf{u}, d\} \in \mathcal{U} \times \mathcal{D} \text{ is stable if and only if}
$$

$$
\forall \{\tilde{\mathbf{u}}, \tilde{d}\} \in \widetilde{\mathcal{U}} \times \widetilde{\mathcal{D}}, \ \exists \bar{h} > 0 : \forall h \in [0, \bar{h}], \ \mathcal{I}(\mathbf{u}, d) \leq \mathcal{I}(\mathbf{u} + h\tilde{\mathbf{u}}, d + h\tilde{d}), \tag{2.11}
$$

with the initial condition $d(\mathbf{x}, 0) = 0$.

The variational inequality (2.11) is satisfied if the Gâteaux derivative of the functional $\mathcal{I}$ at $\{\mathbf{u}, d\}$ is positive for each set of test functions, in particular with $\tilde{d}$ being in the convex cone defined by $\widetilde{\mathcal{D}}$. Formally we write

$$
\mathcal{DI}(\mathbf{u}, d)[\tilde{\mathbf{u}}, \tilde{d}] \geq 0 \quad \forall \{\tilde{\mathbf{u}}, \tilde{d}\} \in \widetilde{\mathcal{U}} \times \widetilde{\mathcal{D}}, \tag{2.12}
$$

with

$$
\mathcal{DI}(\mathbf{u}, d)[\tilde{\mathbf{u}}, \tilde{d}] = \int_{\Omega_0} (\mathbf{S} \cdot \nabla \tilde{\mathbf{u}} - \Sigma \tilde{d} + \mathbf{q} \cdot \nabla \tilde{d}) - \int_{\Omega_0} \mathbf{b}_0 \cdot \tilde{\mathbf{u}} + \int_{\Omega_0^t} \mathbf{t}_0 \cdot \tilde{\mathbf{u}}, \tag{2.13}
$$

where the dual quantities $\mathbf{S}$, Σ and $\mathbf{q}$ are obtained from the energy density (2.3) as

$$
\mathbf{S} = \frac{\partial \psi}{\partial \mathbf{F}} = \omega \sum_{i=1}^{2} \phi_{,i} \, \mathbf{n}_i \otimes \mathbf{N}_i \quad \text{(Piola stress tensor)}, \tag{2.14}
$$

$$
\Sigma = -\frac{\partial \varphi}{\partial d} = -\omega' \phi - \frac{G_c}{\pi b} \eta' \quad \text{(energy release rate density)} \tag{2.15}
$$

and

$$
\mathbf{q} = \frac{\partial \varphi}{\partial \nabla d} = \frac{2 G_c b}{\pi} \nabla d \quad \text{(damage flux vector)}, \tag{2.16}
$$

the Piola stress $\mathbf{S}$ being given by the constitutive equation (2.10) in terms of the principal stretches λ_1 and λ_2.

Upon substitution of (2.14)–(2.16) into (2.13) and integration by parts, the variational inequality (2.12) gives

$$
\int_{\Omega_0} (\text{Div } \mathbf{S} + \mathbf{b}_0) \cdot \tilde{\mathbf{u}} + \int_{\partial \Omega_0^t} (\mathbf{t}_0 - \mathbf{S}\mathbf{n}) \cdot \tilde{\mathbf{u}} = 0 \tag{2.17}
$$

and

$$
-\int_{\Omega_0} (\text{Div } \mathbf{q} + \Sigma) \tilde{d} + \int_{\partial \Omega_0} (\mathbf{q} \cdot \mathbf{n}) \tilde{d} \geq 0, \tag{2.18}
$$

where the latter is evaluated as an inequality since $\tilde{d}$ belongs to the convex cone $\widetilde{\mathcal{D}}$.

By the classical localization argument, we obtain from (2.17) the standard macroscopic balance equation with boundary conditions,

$$\left.\begin{array}{ll} \text{Div } \mathbf{S} + \mathbf{b}_0 = \mathbf{0} & \text{on } \Omega_0, \\ \mathbf{S}\mathbf{n} = \mathbf{t} & \text{on } \partial\Omega_0^t, \end{array}\right\} \tag{2.19}$$

and from (2.18) the damage threshold condition

$$\left.\begin{array}{ll} \text{Div } \mathbf{q} + \Sigma \leq 0 & \text{on } \Omega_0, \\ \mathbf{q} \cdot \mathbf{n} \geq 0 & \text{on } \partial\Omega_0, \end{array}\right\} \tag{2.20}$$

with the corresponding flux condition on the boundary.

On using the definitions of the energy release rate (2.15) and the damage flux vector (2.16), we can rewrite the damage threshold condition $(2.20)_1$ as

$$f(\nabla\mathbf{u}, d, \Delta d) := \frac{G_c}{\pi}\left(2b\Delta d - \frac{1}{b}\eta'(d)\right) - \omega'(d)\psi_0(\mathbf{I} + \nabla\mathbf{u}) \leq 0, \tag{2.21}$$

where we have defined the so-called *damage yield function* f. In the interior region where damage has yet to occur, one has $\omega'(0)\psi_0(\mathbf{I} + \nabla\mathbf{u}) > -(G_c/\pi b)\eta'(0)$ and, since $\omega'(d) < 0$, the elastic energy density ψ_0 is bounded.

We remark once more that the damage threshold condition (2.21) is actually a necessary condition for the state $\{\mathbf{u}, d\}$ to be stable. Indeed, if (2.21) is satisfied everywhere in the domain as a strict inequality, then the derivative (2.12) is strictly positive and $\{\mathbf{u}, d\}$ is a stable state; on the other hand, if there are points at which the damage yield function is zero, then the stability of the state is given by the second derivative of the functional $\mathcal{I}$. This latter case will be discussed in §3 for the one-dimensional problem of a bar under traction.

(ii) Energy balance

On assuming that the evolution is smooth in time, the energy balance principle requires that the rate of change of the internal energy equal the work done by external forces at each time instant, that is,

$$\frac{\mathrm{d}}{\mathrm{d}t}\int_{\Omega_0}\varphi(\nabla\mathbf{u}, d, \nabla d) = \int_{\Omega_0}\mathbf{b}_0 \cdot \dot{\mathbf{u}} + \int_{\Omega_0^t}\mathbf{t}_0 \cdot \dot{\mathbf{u}}, \tag{2.22}$$

which, upon using the macroscopic balance (2.19), gives

$$\int_{\Omega_0} -(\text{Div } \mathbf{q} + \Sigma)\,\dot{d} + \int_{\partial\Omega_0}(\mathbf{q} \cdot \mathbf{n})\,\dot{d} = 0. \tag{2.23}$$

Since each integrand is non-negative by the balance equation (2.20) and the damage irreversibility condition requires that $\dot{d} \geq 0$, the above energy balance equation is satisfied if its integrands vanish. These requirements give the Kuhn–Tucker conditions for the threshold function (2.21):

and

$$\left.\begin{array}{ll} f(\nabla\mathbf{u}, d, \Delta d) = 0 & \text{if } \dot{d} > 0 \\ f(\nabla\mathbf{u}, d, \Delta d) < 0 & \text{if } \dot{d} = 0, \end{array}\right\} \tag{2.24}$$

supplemented by the Neumann-type boundary condition $\nabla d \cdot \mathbf{n} = 0$ on $\partial\Omega_0$.

Remark 2.1 (Evolution problem). The evolution problem arising from the stability condition and energy balance is usually solved numerically in an incremental form. The problem is discretized in time, and at each time step the rates $\{\dot{\mathbf{u}}, \dot{d}\}$ are computed through a staggered minimization scheme obtained by alternating the minimization between $\dot{\mathbf{u}}$ and $\dot{d}$, keeping the other variable constant. This numerical procedure is a standard approach to solving variational problems like the present one (see for instance [49]).

Remark 2.2 (Energy dissipation). The second principle of thermodynamics requires that for each admissible state $\{\mathbf{u}, d\}$, the external work be equal to or greater than the rate of change of the free energy, i.e.

$$\delta = \int_{\Omega_0} \mathbf{b}_0 \cdot \dot{\mathbf{u}} + \int_{\Omega_0^t} \mathbf{t}_0 \cdot \dot{\mathbf{u}} - \frac{\mathrm{d}}{\mathrm{d}t} \int_{\Omega_0} \mathcal{F} \geq 0, \tag{2.25}$$

where $\mathcal{F} = \mathcal{F}(\nabla \mathbf{u}, d, \nabla d)$ is the free-energy density. On using the energy balance equation (2.22) and the definitions (2.3) and (2.14)–(2.16), the dissipation inequality (2.25) is satisfied if

$$\left(\mathbf{S} - \frac{\partial \mathcal{F}}{\partial \mathbf{F}} \right) \cdot \nabla \dot{\mathbf{u}} - \left(\Sigma + \frac{\partial \mathcal{F}}{\partial d} \right) \dot{d} + \left(\mathbf{q} - \frac{\partial \mathcal{F}}{\partial \nabla d} \right) \cdot \nabla \dot{d} \geq 0. \tag{2.26}$$

If we assume that $\mathbf{S}$ and $\mathbf{q}$ are energetic, i.e.

$$\mathbf{S} = \frac{\partial \mathcal{F}}{\partial \mathbf{F}} \quad \text{and} \quad \mathbf{q} = \frac{\partial \mathcal{F}}{\partial \nabla d}, \tag{2.27}$$

and that Σ is made of elastic and dissipative terms,

$$\Sigma = \Sigma_{\mathrm{el}} + \Sigma_{\mathrm{diss}} \quad \text{with} \quad \Sigma_{\mathrm{el}} = -\frac{\partial \mathcal{F}}{\partial d} \text{ and } \Sigma_{\mathrm{diss}} = -\frac{G_c}{\pi b} \eta', \tag{2.28}$$

then inequality (2.26) reduces to

$$\frac{G_c}{\pi b} \eta' \dot{d} \geq 0, \tag{2.29}$$

which is satisfied since $\eta' = 2(1 - d) \geq 0$ from the definition in equation (2.7). By comparing (2.27) and (2.28) with (2.14)–(2.16), we obtain the following expression for the free-energy density:

$$\mathcal{F}(\mathbf{u}, d, \nabla d) = \psi(\mathbf{I} + \nabla \mathbf{u}, d) + \frac{1}{\pi} G_c b |\nabla d|^2. \tag{2.30}$$

Here, by following the approach in [33], we have assumed that the damage non-local energy is stored. However, its thermodynamic nature is still under debate. In [23,24,46] it is assumed to be a dissipative term. This assumption is motivated by the fact that the sum of the second and third terms in (2.3) tends to the fracture energy as the internal length b goes to zero.

Remark 2.3 (Internal length). The internal length b in equation (2.3) can be related to the damage bandwidth ℓ_f at complete fracture, that is, the support of the damage function when $\max\{d\} = 1$, by solving the equilibrium problem of a fractured bar with a passing-through transversal crack. In this case, strains vanish because the bar is broken into two parts, and the strain energy density ϕ nullifies. Thus the balance equation $(2.24)_1$ reduces to $2b\Delta d - (1/b)\eta'(d) = 0$. On integrating it over a line orthogonal to the crack surface (see [22] or [17] for details of the calculation), one obtains

$$b = \frac{\ell_f}{2 \int_0^1 1/\sqrt{\eta(d)} \, \mathrm{d}d},$$

which, by assuming the quadratic expression of $\eta(d)$ in (2.7), reduces to

$$b = \frac{\ell_f}{\pi}. \tag{2.31}$$

(d) Recap of all modelling equations

By following the classical approach to variational fracture mechanics enunciated in principles 1–3 of §2c, we have arrived at equations governing the macroscopic balance,

9

royalsocietypublishing.org/journal/rsta *Phil. Trans. R. Soc. A* **380**: 20210323

$$\begin{array}{ll}\text{macroscopic balance:} & \text{Div } \mathbf{S} + \mathbf{b}_0 = \mathbf{0} \quad \text{on } \Omega_0, \\ & \mathbf{S}\mathbf{n} = \mathbf{t}_0 \quad \text{on } \partial\Omega_0, \end{array} \tag{2.32}$$

together with Kuhn–Tucker conditions for the damage evolution problem,

$$\begin{array}{ll}\text{damage irreversibility:} & \dot{d}(\mathbf{x}, t) \geq 0, \\ \text{damage threshold:} & f(\nabla\mathbf{u}, d, \Delta d) \leq 0, \\ \text{energy balance:} & f(\nabla\mathbf{u}, d, \Delta d)\,\dot{d} = 0, \end{array} \tag{2.33}$$

with initial condition $d(\mathbf{x}, 0) = 0$. The Piola stress tensor $\mathbf{S}$ and the damage threshold function f are

$$\left.\begin{array}{l} \mathbf{S} = \omega \displaystyle\sum_{i=1}^{2} \phi_{,i}\, \mathbf{n}_i \otimes \mathbf{N}_i \\[4mm] f = G_c \left(\dfrac{2}{\pi^2}\ell_f \Delta d - \dfrac{1}{\ell_f}\eta' \right) - \omega'\phi, \end{array}\right\} \tag{2.34}$$

and

where $\mathbf{n}_i$ and $\mathbf{N}_i$ are eigenvectors of the left and right Cauchy–Green strain tensors and

$$\left.\begin{array}{l} \phi = \displaystyle\sum_{n=1}^{N} \dfrac{\mu_n}{\alpha_n}(\lambda_1^{\alpha_n} + \lambda_2^{\alpha_n} + (\lambda_1\lambda_2)^{-\alpha_n} - 3), \\[4mm] \omega = \dfrac{(1-d)^2}{(1-d)^2 + a_1 d(1 + a_2 d + a_2 a_3 d^2)} \\[4mm] \eta = 2d - d^2. \end{array}\right\} \tag{2.35}$$

and

The constitutive parameters included in the formulation are the elastic moduli μ_n, the exponents α_n of the strain energy density ϕ, the fracture energy release rate G_c, the internal length ℓ_f and the polynomial coefficients a_1, a_2 and a_3 of the degradation function ω. In §3e, strategies to calibrate the constitutive parameters are discussed.

3. One-dimensional tension test

In order to fully exploit the capabilities of the proposed model, we now study the problem of a bar under tension. Such a simplified example will allow us to solve the governing equations in semi-analytical form and assess thoroughly the role of the different constitutive coefficients that appear in the model.

(a) Problem definition

We consider a bar of length ℓ and cross-section area $\mathcal{A}_0$. The reference configuration is described through a triad of orthonormal vectors, $\{\mathbf{e}_1, \mathbf{e}_2, \mathbf{e}_3\}$, with $\mathbf{e}_1$ being the main axis of the bar and $\mathbf{e}_3$ the thickness direction, i.e.

$$\Omega_0 = \{\mathbf{x} : \mathbf{x} = x_1\mathbf{e}_1 + x_2\mathbf{e}_2 + x_3\mathbf{e}_3,\ x_1 \in (0, \ell),\ (x_2, x_3) \in \mathcal{A}_0\}.$$

To solve the equilibrium problem, we make the following *ansatz* on the deformation gradient:

$$\mathbf{F}(x_1) = \lambda(x_1)\mathbf{e}_1 \otimes \mathbf{e}_1 + \frac{1}{\sqrt{\lambda(x_1)}}(\mathbf{e}_2 \otimes \mathbf{e}_2 + \mathbf{e}_3 \otimes \mathbf{e}_3), \tag{3.1}$$

such that the principal stretches are $\lambda_1 = \lambda(x_1)$ and $\lambda_2 = \lambda_3 = (\lambda(x_1))^{-1/2}$, $J = 1$, and all fields depend only on the longitudinal coordinate x_1, which from now on we call x without risk of confusion.

The displacement of the bar axis is $u(x)$, and the longitudinal stretch $\lambda(x)$ can be computed from the latter via

$$\lambda(x) = 1 + u'(x), \tag{3.2}$$

with the boundary conditions

$$u(0) = 0 \quad \text{and} \quad u(\ell) = \varepsilon \ell, \tag{3.3}$$

where $\varepsilon \geq 0$ is a control parameter that represents the dimensionless displacement applied at the right end of the bar. In (3.2), we have indicated with a prime $'$ the derivative with respect to the variable x.

We assume the damage field to be constant within the bar cross-section, so that it depends only on the abscissa x, i.e. $d = d(x)$, and satisfies homogeneous boundary conditions at both ends, i.e.

$$d(0) = d(\ell) = 0, \tag{3.4}$$

meaning that no crack can appear at the extremities. Indeed, cracks near the clamping are avoided in the experiments by using dog-bone-shaped specimens.

In this one-dimensional setting, the energy density of the bar takes the form

$$\varphi(\lambda, d, d') = \omega(d)\hat{\phi}(\lambda) + G_c \left(\frac{1}{\ell_f} \eta(d) + \frac{\ell_f}{\pi^2} d'^2 \right), \tag{3.5}$$

where we denote by $\hat{\phi}(\lambda) = \phi(\lambda, \lambda^{-1/2})$ the reduced strain energy density of the bulk solid defined in equation (2.9) as a function of the only variable λ. For the sake or readability the hat will be dropped in the following.

The stress field corresponding to the deformation gradient (3.1) can be computed from (2.10) by substituting $\lambda_1 = \lambda$ and $\lambda_2 = \lambda^{-1/2}$ and noting that the right and left eigenvectors coincide, i.e. $\mathbf{n}_1 = \mathbf{N}_1 = \mathbf{e}_1$ and $\mathbf{n}_2 = \mathbf{N}_2 = \mathbf{e}_2$. The only non-zero component of the Piola stress is the one directed along the bar main axis, i.e. $S = \mathbf{S}\mathbf{e}_1 \cdot \mathbf{e}_1$, with

$$S = \omega\phi', \tag{3.6}$$

which, by applying the definition of Ogden's strain energy density, gives

$$S = \omega \sum_{n=1}^{N} \frac{\mu_n}{\lambda} \left(\lambda^{\alpha_n} - \lambda^{-(\alpha_n/2)} \right).$$

The macroscopic balance equation (2.19) can be rewritten as

$$S'(x) = 0, \tag{3.7}$$

meaning that the stress is constant along the bar. The reduced damage threshold condition (2.33)$_2$ with the deformation (3.1) yields the following form of the one-dimensional threshold function:

$$f(\lambda, d, d'') = G_c \left(\frac{2\ell_f}{\pi^2} d'' - \frac{1}{\ell_f} \eta'(d) \right) - \omega'(d)\phi(\lambda) \leq 0. \tag{3.8}$$

(b) Incremental evolution

Following the analysis in [50], we now solve the incremental evolution problem for both displacement and damage variables starting from a known solution $\{u, d\}$ achieved at a certain time instant t. In doing so, we assume a uniform discretization of the time axis, let τ be the time step and expand both displacement and damage fields to first order in τ:

$$u(x, t + \tau) = u(x, t) + \tau \dot{u}(x, t) \quad \text{and} \quad d(x, t + \tau) = d(x, t) + \tau \dot{d}(x, t), \tag{3.9}$$

such that

$$\dot{u}(0, t) = 0, \quad \dot{u}(\ell, t) = \dot{\varepsilon}\ell, \quad \dot{d}(0, t) = 0 \quad \text{and} \quad \dot{d}(\ell, t) = 0, \tag{3.10}$$

where $\dot{\varepsilon}$ is the rate of the applied displacement at the right end of the bar.

At each time instant the solution of the incremental problem requires the evaluation of the unknown rates $\{\dot{u}, \dot{d}\}$ obtained by imposing the stability condition (2.12) and the energy balance condition (2.24) for the solution $\{u + \tau \dot{u}, d + \tau \dot{d}\}$.

The total energy functional (2.8), with null volume forces, is expanded to second order as

$$\mathcal{I}(u + \tau \dot{u}, d + \tau \dot{d}) \simeq \mathcal{I}(u, d) + \tau \dot{\mathcal{I}}(u, d, \dot{u}, \dot{d}) + \frac{1}{2}\tau^2 \ddot{\mathcal{I}}(u, d, \dot{u}, \dot{d}) = \mathcal{I}(u, d) + \tau \mathcal{J}(\dot{u}, \dot{d}), \tag{3.11}$$

in which we have defined the following functional of the displacement and damage rates:

$$\mathcal{J}(\dot{u}, \dot{d}) = \mathcal{A}_0 \int_0^\ell \left[\omega \phi' \dot{u}' + \left(\omega' \phi + \frac{G_c}{\ell_f} \eta' \right) \dot{d} + \frac{2}{\pi^2} G_c \ell_f d' \dot{d}' \right] dx$$

$$+ \frac{1}{2} \tau \mathcal{A}_0 \int_0^\ell \left[\omega \phi'' \dot{u}'^2 + \left(\omega'' \phi + \frac{G_c}{\ell_f} \eta'' \right) \dot{d}^2 + 2\omega' \phi' \dot{u}' \dot{d} + \frac{2}{\pi^2} G_c \ell_f \dot{d}'^2 \right] dx. \tag{3.12}$$

Stability and energy balance, expressed by relations (2.12) and (2.22) in the three-dimensional formulation of §2, are rewritten in the form

$$\left. \begin{array}{ll} \mathcal{D}\mathcal{J}(\dot{u}, \dot{d})[\tilde{\dot{u}}, \tilde{\dot{d}}] \geq 0 & \text{for any } \{\tilde{\dot{u}}, \tilde{\dot{d}}\} \text{ such that } \tilde{\dot{u}} = \tilde{\dot{d}} = 0 \text{ at } x = 0, l \text{ and } \tilde{\dot{d}} \geq 0 \\ \text{and} \quad \dfrac{d}{d\tau} \mathcal{I}(u + \tau \dot{u}, d + \tau \dot{d}) = \dfrac{d}{d\tau}(\tau \mathcal{J}(\dot{u}, \dot{d})) = 0. \end{array} \right\} \tag{3.13}$$

By performing calculations analogous to those in §2c to deduce the governing equations (2.19) and (2.20) from the stability condition (2.12) and the evolution relations (2.24) from the energy balance (2.22), we obtain the macroscopic evolution equation

$$S' + \tau \dot{S}' = \frac{d}{dx}(\omega \phi') + \tau \frac{d}{dx}(\omega \phi'' \dot{u}' + \omega' \phi' \dot{d}) = 0, \tag{3.14}$$

together with the set of Kuhn–Tucker conditions that govern the evolution of the damage field,

$$\dot{d} \geq 0, \quad f + \tau \dot{f} \leq 0 \quad \text{and} \quad (f + \tau \dot{f})\dot{d} = 0, \tag{3.15}$$

with $\dot{f}$ computed from (3.8) as

$$\dot{f} = -\omega' \phi' \dot{\lambda} - \left(\frac{G_c}{\ell_f} \eta'' + \omega'' \phi \right) \dot{d} + \frac{2}{\pi^2} G_c \ell_f \dot{d}''. \tag{3.16}$$

These conditions state that at each point, the damage can increase only if the yield function $f + \tau \dot{f}$ is equal to zero.

(c) Damage onset

At the beginning of the loading process the damage is zero and the bar is stretched elastically. The balance equation (3.7) shows that the stress and the corresponding deformation are homogeneous along the bar. In this initial phase the damage yield condition (3.8) is not satisfied, i.e. $f < 0$.

The elastic stage terminates when damage appears, meaning that $f = 0$ somewhere along the bar. The stretch λ_o corresponding to the damage onset is evaluated from (3.8) as

$$\phi(\lambda_o) = -\frac{G_c}{\ell_f} \frac{\eta'(0)}{\omega'(0)}. \tag{3.17}$$

At this time instant, say t_o, one can solve the incremental evolution problem of §3b by assuming the following form of the series expansion (3.9):

$$u(x, t_o + \tau) = \varepsilon(t_o)x + \tau \dot{u}_o(x) \quad \text{and} \quad d(x, t_o + \tau) = \tau \dot{d}_o(x), \tag{3.18}$$

since the stretch at the onset is homogeneous, $\lambda_o = 1 + \varepsilon(t_o)$, and the damage is null, $d(x, t_o) = 0$; in addition, $\dot{u}_o$ and $\dot{d}_o$ satisfy the boundary conditions (3.10). At the step $t_o + \tau$, the stretch becomes $\lambda(x, t_o + \tau) = 1 + \varepsilon_o + \tau \dot{\lambda}_o(x)$, so that $\dot{\lambda}_o(x) = \dot{u}_o'(x)$, which is a function of x due to the varying

13

royalsocietypublishing.org/journal/rsta   *Phil. Trans. R. Soc. A* **380**: 20210323

damage profile. A subscript 'o' is used to indicate, here and henceforth, that the corresponding variable is evaluated at time t_o.

The incremental stress in the bar is approximated at first order in τ from the definition of the one-dimensional Piola stress (3.6),

$$S = \omega(\tau \dot{d}_o)\phi'(\lambda_o + \tau \dot{\lambda}_o) \simeq S_o + \tau \dot{S}_o, \tag{3.19}$$

with

$$S_o = \phi_o' \quad \text{and} \quad \dot{S}_o = \omega_o \phi_o' \dot{d}_o + \phi_o'' \dot{\lambda}_o. \tag{3.20}$$

Since the zeroth-order stress S_o is constant along the bar, the macroscopic balance (3.14) yields $(\dot{S}_o)' = 0$, meaning that $\dot{S}_o$ is also homogeneous. The damage threshold condition $f = 0$ is satisfied at both $t = t_o$ and $t = t_o + \tau$, so the incremental threshold (3.15) is zero at both zeroth and first orders; the latter gives

$$\frac{2}{\pi^2} G_c \ell_f \dot{d}_o''(x) - \left(\omega_o'' \phi_o + \frac{G_c}{\ell_f} \eta_o'' \right) \dot{d}_o(x) = \phi_o' \dot{\lambda}_o(x), \tag{3.21}$$

which is, indeed, a second-order differential equation for the damage rates $\{\dot{\lambda}_o, \dot{d}_o\}$. The right-hand side of (3.21) can be transformed by using the definition of $\dot{S}_o$ in (3.20); after some manipulations we arrive at a differential equation in terms of the variable $\dot{d}_o$,

$$\frac{2}{\pi^2} G_c \ell_f \dot{d}_o''(x) - j \dot{d}_o(x) = \frac{\omega_o' \phi_o'}{\phi_o''} \dot{S}_o, \quad \text{with } j = \omega_o'' \phi_o - \frac{\omega_o'^2 \phi_o'^2}{\phi_o''} + \frac{G_c}{\ell_f} \eta_o'', \tag{3.22}$$

where the right-hand side is now independent of x. If we introduce the internal lengths

$$\ell_i = 2\sqrt{\frac{2 G_c \ell_f}{|j|}} \quad \text{and} \quad \ell_s = \frac{\omega_o'^2 \phi_o'^2}{\phi_o'' |j|} \ell_i, \tag{3.23}$$

equation (3.22) can be rewritten in the form

$$\dot{d}_o''(x) - \text{sign}(j) \left(\frac{2\pi}{\ell_i} \right)^2 \dot{d}_o(x) = \left(\frac{2\pi}{\ell_i} \right)^2 \sqrt{\frac{\ell_s}{\ell_i}} \frac{\dot{S}_o}{\sqrt{\phi_o'' |j|}}, \tag{3.24}$$

which is a second-order differential equation in the variable x of the unknown rate $\dot{d}_o$ to be solved with the boundary conditions $\dot{d}_o(0) = 0$ and $\dot{d}_o(\ell) = 0$. The analytical approach used to solve this equation, as well as the expressions for the solutions, can be found in the appendix. According to the sign of j and, in the case of $j < 0$, the ratios ℓ/ℓ_i and ℓ/ℓ_s, different solutions are found. A schematic of the different regimes is given in figure 1. It is possible to distinguish *full-size* and *localized* fracture initiations, depending on whether the support of $\dot{d}_o$ is the entire bar or a sub-region of length $\ell_i < \ell$. Moreover, the evolution regime can be *stress-hardening* if $\dot{S}_o > 0$, or *stress-softening* if $\dot{S}_o < 0$. As shown in figure 1, for $j < 0$, four different regions are found in the plane $(\ell/\ell_i, \ell/\ell_s)$, each characterized by a different damage evolution.

In the case of the localized solution (region c), the bar must be longer than ℓ_i to have damage localization in a sub-region of length ℓ_i, and must be shorter than ℓ_s to avoid brittle failure. These requirements express the size sensitivity of the model: as the size of the bar increases, the response moves from pseudo-ductile to brittle. If we suppose damage localization at t_o, the slope k_o of the curve $S = S(\varepsilon)$ is obtained from equation (A 4)$_2$ as

$$k_o = \left. \frac{\mathrm{d}S}{\mathrm{d}\varepsilon} \right|_{t_o} = \frac{\dot{S}_o}{\dot{\varepsilon}_o} = \frac{\omega_o \phi_o''}{1 - \ell_s/\ell}, \tag{3.25}$$

which has a negative value and decreases as ℓ increases; in particular $k_o \to -\infty$ for $\ell \to \ell_s$.
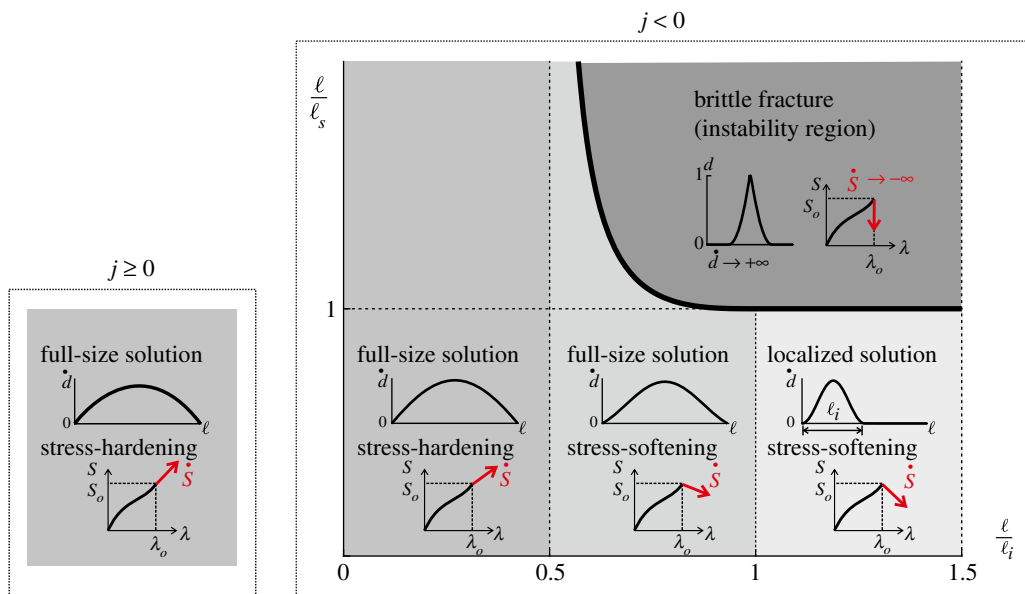
Figure 1. Different damage evolution regimes obtained from equation (3.24) for $j \geq 0$ (left) and $j < 0$ (right). (Online version in colour.)

On integrating (A 1) over $(0, \ell)$ and rearranging the terms, we obtain the displacement rate at the end-section,

$$\dot{u}_o(\ell) = \ell \dot{\varepsilon}_o = \dot{v}_o + \dot{w}_o \quad \text{with } \dot{v}_o = \ell \frac{\dot{S}_o}{\phi_o''} \text{ and } \dot{w}_o = -\frac{\omega_o' \phi_o'}{\phi_o''} \int_0^\ell \dot{d}_o \, dx, \tag{3.26}$$

which is the sum of two contributions: $\dot{v}_o$ is the displacement rate due to elastic stretching, and $\dot{w}_o$ is the displacement rate induced by the fracture opening. In the case of localized $\dot{d}_o$ (case c, with $\ell_i \leq \ell \leq \ell_s$), the fracture opening rate is

$$\dot{w}_o = \frac{\ell_s}{1 - \ell_s/\ell} \dot{\varepsilon}_o. \tag{3.27}$$

Let $w = w(t)$ be the displacement accounting for fracture opening in a fracture evolution process. Using (A 4)$_2$ and (3.27), we can evaluate the derivative of S with respect to w at fracture initiation as

$$\hat{k}_o = \frac{dS}{dw}\bigg|_{t_o} = \frac{\dot{S}_o}{\dot{w}_o} = -\frac{\phi_o''}{\ell_s}. \tag{3.28}$$

The coefficient $\hat{k}_o$ represents the initial slope of the so-called *cohesive curve* $S = S(w)$, which describes the specific failure mode of the material. Since the cohesive law $S = S(w)$ is an intrinsic property of the material, $\hat{k}_o$ does not depend on the length ℓ, in contrast to (3.25).

(d) Cohesive fracture

In this section, we define a strategy to estimate the cohesive curve $S = S(w)$ that characterizes the fracture opening process. The function $S(w)$ is usually assigned *a priori* in standard formulations of cohesive fracture mechanics [51,52], whereas in the proposed variational approach it is obtained from the particular form of the fracture energy.

We suppose that at a certain time instant of the evolution process, damage is localized in a sub-region $(0, 2x^*)$, with $x^* < \ell/2$ the half-bandwidth length, and that it has attained the maximum value d^* at $x = x^*$. The proposed procedure allows us to determine the length x^*, the stress S,

the functions d and λ, the fracture opening w, and the corresponding strain ε in terms of d^* by integrating the balance equations (3.7) and (3.8).

We suppose that at each material point, the stretch λ is the superposition of elastic λ_e and fracture λ_f stretches,

$$\lambda = \lambda_f \lambda_e, \tag{3.29}$$

where λ_e would be the homogeneous stretch obtained from S if d were zero; as such, it can be evaluated from the constitutive equation of the undamaged material by

$$\phi'(\lambda_e) = S. \tag{3.30}$$

The fracture opening w, that is, the displacement at $x = \ell$ produced by the damage occurrence, is

$$w = \int_0^{\lambda_e \ell} (\lambda_f(x_e) - 1) \, \mathrm{d}x_e = \int_0^\ell (\lambda - \lambda_e) \, \mathrm{d}x = (1 + \varepsilon)\ell - \lambda_e \ell. \tag{3.31}$$

Within the damage region $(0, 2x^*)$, the damage threshold condition (3.8) is evaluated as an equality and

$$\omega' \phi + G_c \left(\frac{1}{\ell_f} \eta' - \frac{2\ell_f}{\pi^2} d'' \right) = 0. \tag{3.32}$$

On multiplying all terms by d' and integrating over $(0, x)$ with $x \le x^*$, the previous equation gives

$$G_c \left(\frac{1}{\ell_f} \eta - \frac{2\ell_f}{\pi^2} d'^2 \right) + \int_0^x \frac{\mathrm{d}\omega}{\mathrm{d}\hat{x}} \phi \, \mathrm{d}\hat{x} = 0, \tag{3.33}$$

where the latter term is rewritten upon integration by parts as

$$\int_0^x \frac{\mathrm{d}\omega}{\mathrm{d}\hat{x}} \phi \, \mathrm{d}\hat{x} = \omega \phi - \phi(\lambda_e) - \int_0^x \omega \phi' \frac{\mathrm{d}\lambda}{\mathrm{d}\hat{x}} \, \mathrm{d}\hat{x} = \omega \phi - \phi(\lambda_e) - (\lambda - \lambda_e)S, \tag{3.34}$$

since $S = \omega \phi'$ is constant along the bar. Equation (3.33) becomes

$$G_c \left(\frac{1}{\ell_f} \eta - \frac{2\ell_f}{\pi^2} d'^2 \right) + \omega \phi - \phi(\lambda_e) - (\lambda - \lambda_e)S = 0. \tag{3.35}$$

At $x = x^*$, where the maximum damage is attained, $d'(x^*) = 0$ and the previous equation further simplifies to

$$\frac{G_c}{\ell_f} \eta(d^*) + \omega(d^*)\phi(\lambda^*) - \phi(\lambda_e) - (\lambda^* - \lambda_e)S^* = 0, \tag{3.36}$$

where quantities evaluated at $x = x^*$ are labelled by an asterisk. In (3.36), the stretches λ^* and λ_e are worked out by inversion of the constitutive equations

$$\omega(d^*)\phi'(\lambda^*) - S^* = 0 \quad \text{and} \quad \phi'(\lambda_e) - S^* = 0. \tag{3.37}$$

For any assigned value of $d^* \in [0, 1]$, the triplet $\{\lambda^*, \lambda_e, S^*\}$ solves the set of equations (3.36) and (3.37). Once S^* is determined, the profiles of d and λ at points $x \in [0, x^*]$ can be evaluated from (3.35), here rewritten in the form

$$d' = \frac{1}{\ell_f} h(d, d^*) \quad \text{with } h(d, d^*) := \pi \sqrt{\frac{\ell_f}{G_c} [\omega(d)\phi(\lambda) - \phi(\lambda_e) - f^*(\lambda - \lambda_e)] + \eta}, \tag{3.38}$$

where λ is the solution of the equation

$$\omega(d)\phi'(\lambda) - S^* = 0. \tag{3.39}$$

Upon inversion of equation (3.38), one obtains the expression for x in terms of the damage profile and the maximum damage d^*,

$$x(d, d^*) = \int_0^d \frac{\ell_f}{h(\hat{d}, d^*)} \, \mathrm{d}\hat{d}, \tag{3.40}$$

and the stretch λ at x is the solution of (3.39). The half-bandwidth length is obtained from the above relation by assigning $d = d^*$, giving

$$x^* = \int_0^{d^*} \frac{\ell_f}{h(\hat{d}, d^*)} \, d\hat{d}, \tag{3.41}$$

and the fracture opening w is determined from (3.31) once λ, λ_e and x^* are known. Upon inversion of the equation, the assigned stretch can also be computed:

$$\varepsilon = \lambda_e + \frac{w}{\ell} - 1. \tag{3.42}$$

To conclude, the above procedure can be implemented numerically through the following steps:

(i) Assign the value d^* of the maximum damage.
(ii) Solve equations (3.36) and (3.37) to determine S^*, λ^* and λ_e.
(iii) Discretize the damage range $[0, d^*]$, and for any d_i of the discretized set determine the position x_i from (3.40). The discrete profile of $d = d(x)$ is given by the pairs (x_i, d_i).
(iv) Determine λ_i at point x_i from (3.39). The discrete profile of $\lambda = \lambda(x)$ is formed by points (x_i, λ_i). At points $x > 2x^*$ the stretch is equal to λ_e.
(v) Determine w from (3.31).

This algorithm allows the cohesive curve $S = S(w)$ to be evaluated at discrete points, by iterating the scheme for different $d^* \in [0, 1]$. The damage evolution determined through this procedure is based on the balance equations (3.7) and (3.8). We point out that the numerical simulations of §4 are in fact obtained by solving the full evolution problem of §3b by finite elements. Although the approaches are different, the estimate of the cohesive curve obtained through steps (i)–(v) gave results accurate enough to capture the qualitative behaviour of the model. As such, the proposed numerical scheme represents an useful tool for exploring the variety of damage mechanisms. In the next section, these results are used to assess the effects of the different constitutive parameters on the damage evolution modes. Criteria for parameter calibration will be also discussed.

(e) Physical interpretation of the cohesive parameters

The constitutive coefficients a_1, a_2 and a_3 that appear in the energy degradation function ω, as defined in (2.6), are related to specific properties of cohesive fracture evolution, to give them clear physical meanings and to allow their robust evaluation from the experimental data. In the following calculations, the elastic coefficients μ_n and α_n, the fracture energy release rate G_c and the internal length ℓ_f are assumed to be known.

The coefficients a_1 and a_2 in (2.6) can be tailored from the model response at the damage onset. At this time instant $\lambda_f = 1$, $\lambda_e = \lambda_o$ and the stress S_o is known. Since $d_o = 0$, the functions ω and η at t_o are

$$\eta(0) = 0, \quad \omega(0) = 1, \quad \eta'(0) = 2, \quad \omega'(0) = -a_1,$$

$$\eta''(0) = -2 \quad \text{and} \quad \omega''(0) = 2a_1(a_1 - a_2 - 2).$$

Therefore we have the following.

(1) a_1 is determined by the limit elastic stretch λ_o through relation (3.17), which, once inverted, gives
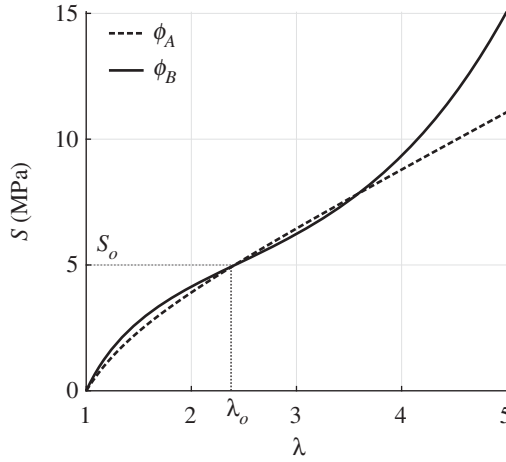
$$a_1 = 2 \frac{G_c}{\phi_o \ell_f}. \tag{3.43}$$

Figure 2. Piola stress S versus (elastic) stretch λ for the two strain energies ϕ_A and ϕ_B.

(2) a_2, which appears in $\omega''(0)$, is made dependent on the slope $\hat{k}_o$ of the cohesive curve (3.28) at the damage onset, i.e.

$$\hat{k}_o = -\frac{\phi_o''^2}{2a_1^2 S_o^2}\sqrt{\frac{|j|^3}{2G_c \ell_f}}, \quad \text{with } j = 2a_1(a_1 - a_2 - 2)\phi_o - \frac{a_1^2 S_o^2}{\phi_o''} - \frac{2G_c}{\ell_f}, \tag{3.44}$$

where j is negative, as the formula is evaluated for the localized damage case (case c in §3c). From (3.44), a_2 has the expression

$$a_2 = \frac{1}{2a_1\phi_o}\left[\left(-\frac{2a_1^2 S_o^2}{\phi_o''^2}\sqrt{2G_c \ell_f}\,\hat{k}_o\right)^{2/3} + 2a_1(a_1 - 2)\phi_o - \frac{a_1^2 S_o^2}{\phi_o''} + \frac{2G_c}{\ell_f}\right]. \tag{3.45}$$

(3) a_3 multiplies the third-order term in the polynomial (2.6), so it mainly influences states with large damage. In [17], in fact, a_3 was related to the displacement jump $\tilde{w}$ at complete fracture of the specimen through the formula

$$a_3 = \frac{1}{a_2}\left[\frac{1}{2}\left(\frac{\tilde{w}S_o}{2G_c}\right)^2 - (1 + a_2)\right]. \tag{3.46}$$

Since this relation was derived within the context of linear elasticity, it cannot be straightforwardly extended to the finite-strain case. Accordingly, it is just used to obtain an estimate of the parameter a_3. For damage occurring at small strains, formula (3.46) provides the exact value to assign to a_3 in order for the fracture jump to be $\tilde{w}$. In contrast, for damage onset at large strains it gives only an approximate value. Further insights can be gained by drawing the cohesive curve, as discussed in the following.

To better highlight the role of the different cohesive parameters, we now consider two different forms of the Ogden elastic strain energy density with different elastic parameters: one with $N = 1$ in the series $(2.35)_1$ and with $\mu_1 = 2.2$ MPa and $\alpha_1 = 2$, which we call quadratic energy ϕ_A, and the other with $N = 2$, $\{\mu_1, \mu_2\} = \{4.8, 0.01\}$ MPa and $\{\alpha_1, \alpha_2\} = \{1.2, 5.1\}$, say ϕ_B. As shown in figure 2, such choices of the elastic coefficients represent two plausible elastic responses of a rubbery material; the former has a linear Piola stress at large stretches, whereas the latter shows the stress-hardening at large stretches typical of elastomers.

The cohesive curves $S = S(w)$ corresponding to these elastic energies are shown in figure 3 for $\ell_f = 5$ mm and different values of the parameters G_c, $\hat{k}_o$ and a_3. For a given G_c, the values of $\hat{k}_o$ and $\tilde{w}$ are assigned by supposing that the cohesive law is linear with respect to the fracture opening,
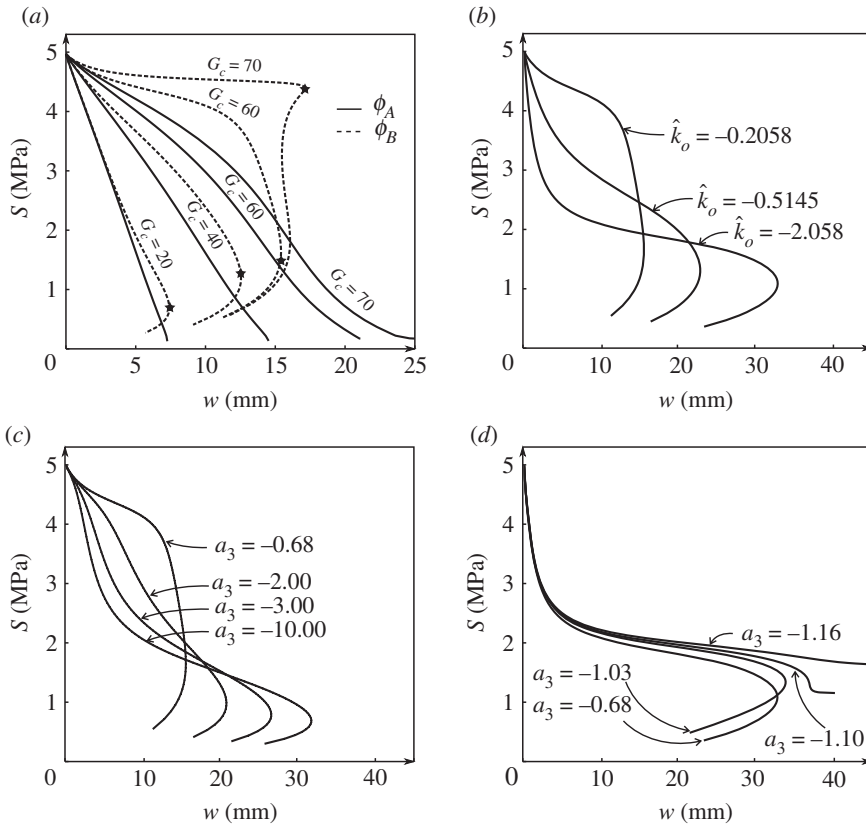
Figure 3. Cohesive curves for (a) different values of the parameter G_c for the energy densities ϕ_A (solid) and ϕ_B (dashed); (b) different $\hat{k}_o$ and fixed $G_c = 60$ MPa and $a_3 = -0.6851$; (c,d) different a_3, fixed $G_c = 60$ MPa and (c) $\hat{k}_o = -0.2058$ MPa mm^{-1} or (d) $\hat{k}_o = -2.0580$ MPa mm^{-1}.

$S = -(S_o^2/2G_c)w + S_o$, an expression which is the simplest triangular cohesive curve. Accordingly, $\hat{k}_o = -S_o^2/2G_c$ and $\tilde{w} = 2G_c/S_o$. The coefficients a_1, a_2 and a_3 are derived from (3.43), (3.45) and (3.46). For small values of G_c, the cohesive curves recover the linear law when the energy density ϕ_A is used, whereas they deviate from linearity as G_c is increased. When the two-term energy density ϕ_B is considered, linearity is lost, as shown by the dashed curves in figure 3a. In this case, the curves initially decrease with smaller slope, attaining larger values of stress. Then they exhibit snap-back branches that are more pronounced for increasing values of G_c. The initial raising of the curve and the presence of a snap-back tail, indicated with a star in the figure, depends on the specific shape of ϕ_B, which has a convex branch where stiffness grows as the stretches increase (see figure 2). This determines the fracture properties of the material. Indeed, the softening process of fracture requires a larger stress for crack opening in the initial stage, and when the snap-back branch is encountered, it stops due to the complete rupture of the specimen. As a consequence, the recovery in the elastic stiffness for large stretches induces an increased stiffness in the initial phase of crack opening and a brittle response in the final stage of the fracture evolution. One way to reduce the snap-back tails in the cohesive curves is to increase the initial slope $\hat{k}_o$. This is shown in figure 3b, where cohesive curves for different values of $\hat{k}_o$ are plotted by keeping the fracture toughness $G_c = 60$ MPa mm and $a_3 = -0.6851$ constant.

Note that the parameter a_3 also influences the softening process, as shown in figure 3c,d. By scrutinizing the curves of figure 3c, one can see that a decrease in $a_3 < 0$ has two distinct effects: (i) the negative slope of the curve is increased in its initial part, and (ii) the displacement w at the snap-back is increased, with the final stage of brittle failure being reduced. The curves in figure 3d

are drawn for a fixed value of $\hat{k}_o$ which is ten times larger than that of the curves in figure 3*c*. In this case, the coefficient a_3 influences the final part of the cohesive curves: large negative values of a_3 raise the curve tail, reducing the snap-back up to its complete disappearance. It turns out that the final catastrophic fracture is replaced by a recovery of stiffness that allows the material to further bear stresses.

As a result, the coefficients a_1 and a_2 can be assigned through formulae (3.43) and (3.45), which relate them to the limit elastic stretch λ_o and to the initial slope of the cohesive curve $\hat{k}_o$, respectively. The calibration of a_3 is more troublesome. The estimate in equation (3.46) gives an initial value for the parameter, yet a more appropriate value can be obtained only after having numerically examined the cohesive curves, such as those in figure 3*c*,*d*. The qualitative behaviour observed for increasing values of a_3 is a stretching of the cohesive curve with consequent reduction or even removal of the final brittle fracture.

We finally remark that the model proposed in [17] is indeed size-independent as shown in [53]. However, in the proposed extension to finite elasticity, this independence is only partially maintained: the fracture activation stress S_o and the initial slope $\hat{k}_o$ of the cohesive curve still do not depend on ℓ_f, but the shape of the softening cohesive curve $S = S(w)$ does. As a result, the convergence of the model to the cohesive fracture is lost, meaning that the model should be interpreted as a damage model in which the internal length is a constitutive parameter representing the length of the transition zone (process zone). Such a parameter may be directly calibrated through *ad hoc* experiments such as the one reported in [54].

4. Numerical examples

The variational model (2.32) and (2.33) was implemented in the finite-element open-source framework FEniCS [55].

The displacement and damage fields were projected over a piecewise-affine finite-element space (Lagrange elements) by using the same mesh domain. As the energy functional $\mathcal{I}$, defined in (2.8) for the general formulation and in (3.11) for the simple tension incremental problem, is separately convex in each variable, an alternating minimization algorithm in the variables u and d was implemented. At a given time step, the solution of the iterative evolution of §3b was achieved by iterating on the following subproblems until convergence.

   (1) The minimization of $\mathcal{I}$ with respect to u at fixed d is an unconstrained optimization problem solved as a nonlinear elastic problem with the prescribed boundary conditions through the Newton–Raphson method.
   (2) The minimization of $\mathcal{I}$ with respect to d at fixed u is a unilateral constrained optimization problem, which was solved using TAO (Tool-kit for Advanced Optimization).

Further details of the numerical implementation can be found in [49]. Simulations on both one-dimensional or two-dimensional geometries were carried out, although the results shown in the paper refer to the latter.

Two numerical examples are discussed in the following. As a first benchmark problem, we consider a rectangular test specimen subjected to tensile loadings. This example has a twofold purpose: assessing the sensitivity of the model with respect to the different constitutive parameters and demonstrating the ability of the proposed modelling framework to capture the large-strain behaviour of double-network elastomers [36]. Afterwards, we use a double-edge notched specimen in tension to validate the model prediction up to the specimen rupture against the experiments on conventional elastomers reported in [56].

The rectangular specimen used to carry out the sensitivity analysis is shown in figure 4 together with boundary conditions and details of the mesh, which was made up of 12 000 Lagrange triangular elements. The height of the specimen was kept fixed at 4 mm, whereas three different lengths were considered, $\ell = 6, 13$ and 20 mm. In all simulations two different sets of elastic parameters were used to assess the effects of the particular form of the Ogden energy on
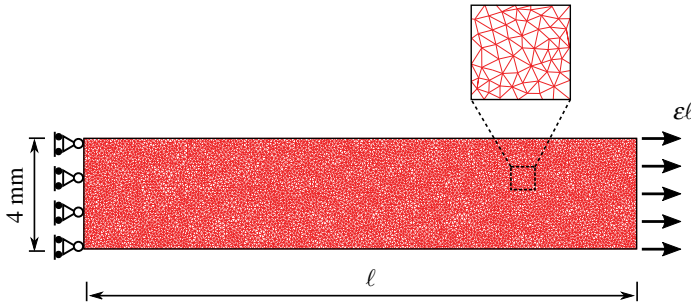
Figure 4. Geometry of the rectangular specimen with details of the mesh composed of about 12 000 Lagrange triangular elements. The height of the specimen was kept fixed in all numerical tests, whereas different lengths $\ell = 6, 13$ and 20 mm were considered. (Online version in colour.)

Table 1. Constitutive parameters used in the numerical examples.

elastic			
ϕ_A:	$\mu_1 = 2.2$ MPa		$\alpha_1 = 2$
ϕ_B:	$\{\mu_1, \mu_2\} = \{4.8, 0.01\}$ MPa		$\{\alpha_1, \alpha_2\} = \{1.2, 5.1\}$
fracture			
	$\ell_f = 5$ mm, $\quad G_c = 60$ MPa mm, $\quad \lambda_o = 2.4, \quad \hat{k}_o = -0.21$ MPa mm^{-1}		
	ϕ_A: $a_3 = -0.57$, $\quad \phi_B$: $a_3 = -0.68$		

the fracture properties of the material, corresponding to the energies ϕ_A and ϕ_B in figure 2; the other constitutive parameters are the ones in table 1 except where stated. We point out that the coefficients a_1, a_2 and a_3 were obtained from G_c, $\hat{k}_o$ and $\tilde{w}$ by using the formulae (3.43), (3.45) and (3.46).

The Piola stress S in terms of the overall strain ε as well as the damage profiles along the mean axis of the bar are plotted in figures 5 and 6 for the two energy densities ϕ_A and ϕ_B and different values of the energy release rate G_c.

By increasing values of G_c, the maximum strain attained at rupture grows with a larger region in which a pseudo-ductile response is achieved. With the energy ϕ_A, the response with $G_c = 20$ MPa mm (green curve in figure 5) shows a sudden drop in the stress caused by an abrupt damage growth at the end of the elastic stage, which almost immediately reaches values close to 1 as shown by the green damage profiles in the figure. The resulting overall behaviour is brittle. For larger values of G_c, the drop in the stress is smoothed out with cohesive-like softening curves; in terms of damage this behaviour is produced by the phase-field variable progressively growing and enlarging.

For the elastic coefficients in the energy ϕ_B, brittle and cohesive responses are obtained for $G_c = 20$ and 40 MPa mm, respectively. For $G_c = 60$ MPa mm, the specimen exhibits a pseudo-ductile behaviour in which two response stages are clearly observed: a softening branch with a low slope, followed by a sudden drop in the stress. As the damage profiles show, in the first stage of moderate softening, the damage grows slowly while expanding through the bar. At the end of this phase, the damage has covered the entire domain and has reached its maximum value of 0.3. Thereafter the damage immediately increases, producing rupture of the specimen with the resulting stress rapidly decreasing to zero.

Since the gradient term in the fracture energy makes the model size-dependent, the effect of specimen length is analysed in figure 7 for $\ell = 6, 13$ and 20 mm. The results indicate that when ℓ
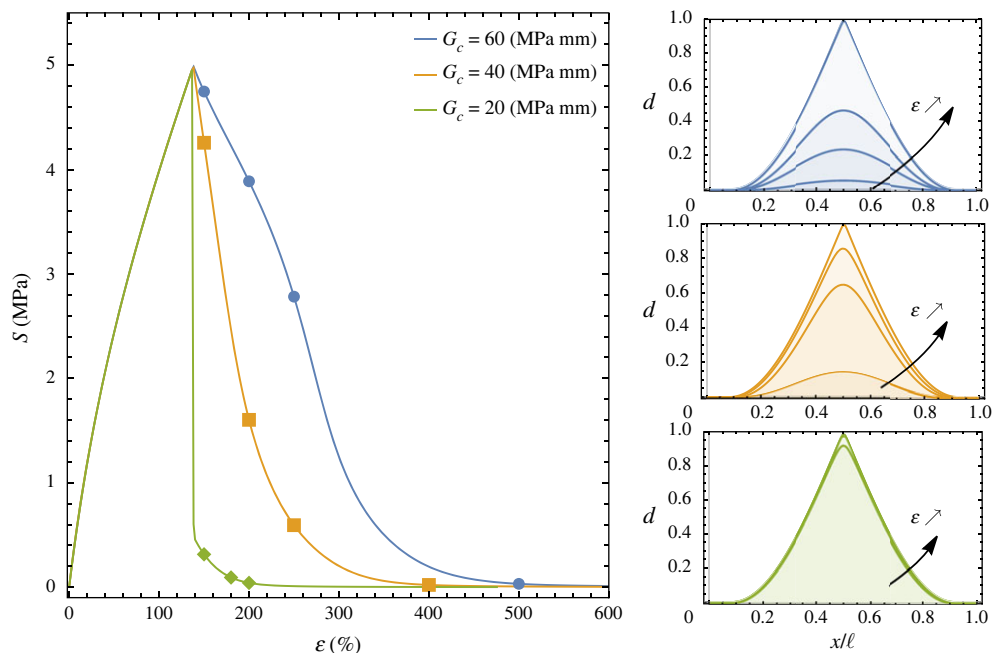
Figure 5. Influence of the energy release rate G_c in the case of the elastic energy ϕ_A: the Piola stress S versus the overall strain ε for $G_c = 20, 40$ and 60 MPa mm. The insets show the damage profiles d evaluated on the mean axis of the bar at the different stretch levels indicated by dots on each curve. (Online version in colour.)
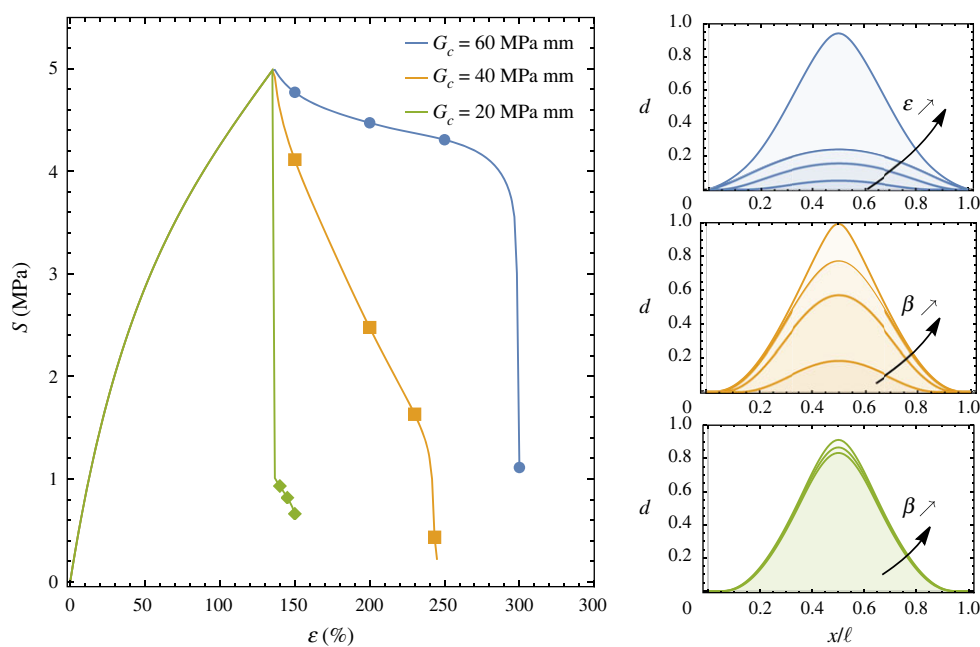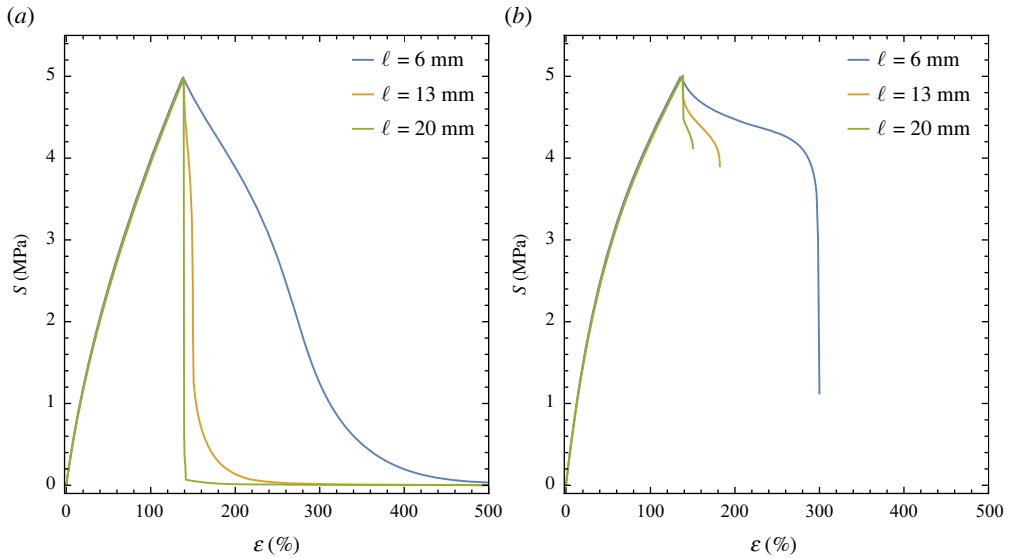

Figure 6. Influence of the energy release rate G_c in the case of the elastic energy ϕ_B: the Piola stress S versus the overall strain ε for $G_c = 20, 40$ and 60 MPa mm. The insets show the damage profiles d evaluated on the mean axis of the bar at the different stretch levels indicated by dots on each curve. (Online version in colour.)

Figure 7. Size dependence of the model: Piola stress versus strain curves for different bar lengths $\ell = 6, 13$ and 20 mm and elastic energies (a) ϕ_A and (b) ϕ_B. (Online version in colour.)

is comparable to the internal length $\ell_f = 5$ mm the response is cohesive, whereas sufficiently long bars display brittle or quasi-brittle failure for both energies ϕ_A (figure 7a) and ϕ_B (figure 7b).

In figure 8, the dependence of the material response on the slope of the cohesive curve $\hat{k}_o$ is also investigated. This constitutive parameter is directly related through equation (3.45) to a_2. As the results show, $\hat{k}_o$ controls the stress decrease at the damage onset and regulates the softening branch with moderate slope, which is associated with a process of damage propagation over the whole domain. Large values of $\hat{k}_o$ may induce snap-back of the cohesive curve, with a subsequent discontinuous drop in the stress. Simulations start with values of $\hat{k}_o$ in table 1 (blue curve in the figure), with cohesive-like behaviour for both energies ϕ_A (figure 8a) and ϕ_B (figure 8b).

Finally, the influence of coefficient a_3 is analysed in figure 9. The green curve corresponds to the value of $a_3 = -0.68$ in figure 8b (with $\hat{k}_o = -2$ MPa mm^{-1}), whereas the other two curves are obtained by increasing a_3 by a factor of 2 and 4, respectively, such that $a_3 \in \{-0.68, -1.36, -2.72\}$. As pointed out in §3e, increasing values of a_3 lead to a recovery of the material stiffness, with a consequent transition from a softening (green curve) to a hardening response (orange and blue curves). In all cases, a significant stress drop is seen at the end of the elastic phase, which corresponds to the sudden occurrence of localized damage in the central part of the specimen, with the phase-field variable reaching 0.2. Thereafter different damage evolution regimes are seen: for the green curve ($a_3 = -0.68$) the damage increases sharply in the central part of the specimen until it reaches the value of 1, meaning that the specimen is completely broken; in contrast, the orange and blue curves show a rather limited increase in the damage intensity, $d < 0.4$, yet the support of the phase-field variable enlarges, up to the point where the damage occupies the entire bar. This type of evolution resembles a sort of 'plastic-wave' that propagates inside the bar (damage wave in this case) and has indeed been observed in double-network elastomers.

As a general remark on the model behaviour, in all simulations it was observed that the rate of damage growth is proportional to the slope of the softening branch. Furthermore, a broadening of the damage localization zone is observed when the softening branch is convex, whereas a concave softening branch produces damage localization in narrow regions.

Having shown the main features of the proposed model, we are now in a position to compare the model prediction with the experimental data on double-network elastomers. The experiments used to calibrate the model are the ones reported in [36], where a cross-linked elastomer was
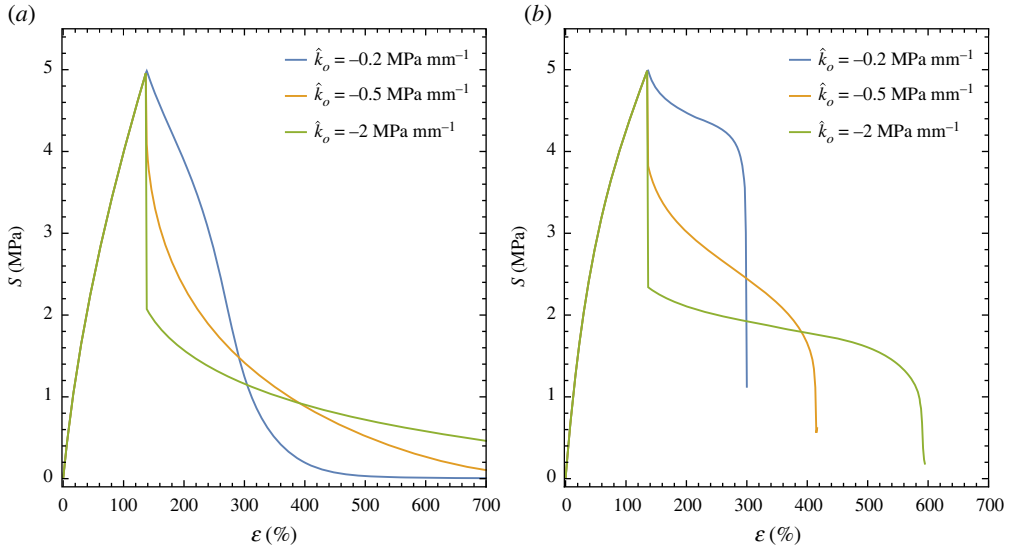
Figure 8. Influence of the cohesive parameters $\hat{k}_o$: Piola stress versus strain curves for different values of the cohesive curve slope, $\hat{k}_o = -0.2$, -0.5 and -2 MPa mm^{-1}, and elastic energies (a) ϕ_A and (b) ϕ_B. (Online version in colour.)
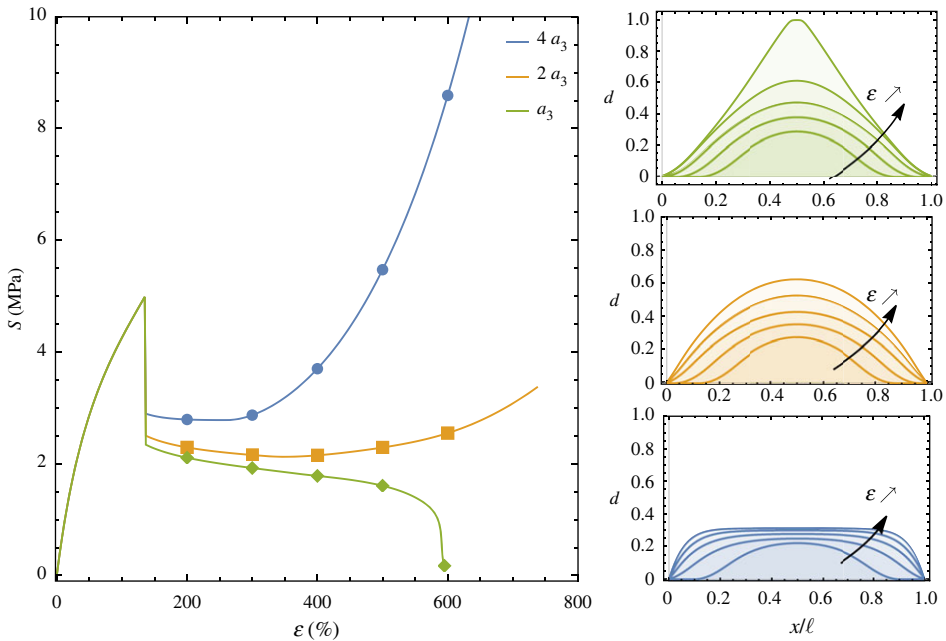

Figure 9. Influence of the fracture parameter a_3: Piola stress versus strain curves for $a_3 = -0.68$, -1.36 and -2.72 with the elastic parameters in ϕ_B. The insets show the damage profile at the different strain levels indicated by dots on the stress–strain curve. (Online version in colour.)

first swollen in monomer and subsequently polymerized to create the so-called double network. This novel class of elastomers displays unique mechanical features due to the combined use of a stretchy matrix with a stiff filler network, which makes the compound fail in a controlled, pseudo-ductile way at large strain.
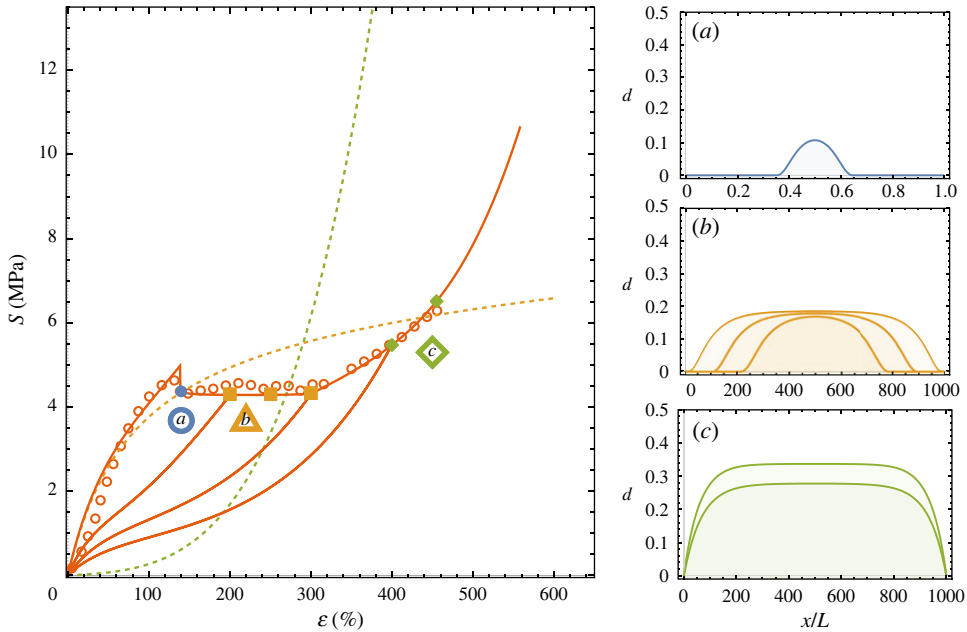
Figure 10. Piola stress S versus overall strain ε for a double-network elastomer: open circles represent experimental data from [36], continuous curves correspond to the model prediction, and dashed curves show the response of the purely elastic model. The fitting is achieved with the model parameters in table 2. The insets show the damage profile along the specimen middle axis at the strain levels (*a*), (*b*) and (*c*) indicated in the plot. (Online version in colour.)

Table 2. Constitutive parameters used for the fitting of the experimental data in figure 10.

elastic	
$\{\mu_1, \mu_2\} = \{4.6, 0.012\}$ MPa	$\{\alpha_1, \alpha_2\} = \{1.2, 5.5\}$
fracture	
$\ell_f = 5$ mm, $G_c = 100$ MPa mm, $\lambda_o = 2.4$, $\hat{k}_o = -0.37$ MPa mm, $a_3 = -4.73$	

These characteristics are readily seen from the data in figure 10 where the Piola stress, S, is plotted against the normalized displacement at the bar's end, ε. The initial part of the curve resembles the typical response of an elastomeric material with pronounced nonlinear elastic behaviour. The elastic phase terminates at about $\varepsilon = 1.4$ where a sharp decrease in the stress appears. Microscopically this drop corresponds to the emergence of a very localized damage region. By continuing loading, the applied force remains constant and the stress–strain plot shows a plateau for a wide range of stretches. The formation of a neck and its propagation along the specimen is observed in this region. When necking has expanded all over the sample, at about $\varepsilon = 4.2$, the damage starts to increase uniformly, yet the overall stiffness of the sample grows. This behaviour reflects a competition between the stress-softening induced by the damage and the stiffening caused by the intact polymer chains being almost completely stretched. Such a peculiar behaviour for an elastomer was reported for the first time in [36].

Remarkably, the proposed model is able to capture the main features seen in the experimental data, as the fitting in figure 10 shows. The stress–strain plot displays three different curves along with the experimental points represented by open orange circles: the continuous orange curve is the output of the model and has all the main characteristics of the experimental response, including the initial nonlinear elastic regime, the stress peak with the subsequent stress plateau
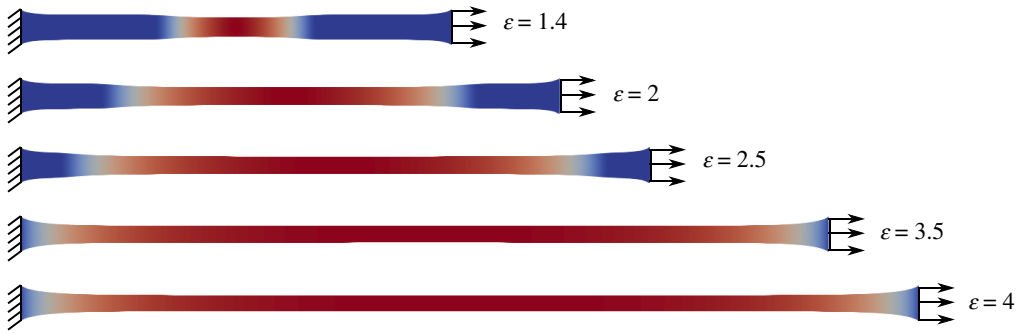
Figure 11. Deformed configuration of the rectangular specimen used for fitting the data in figure 10. The plateau in the stress–strain curves corresponds to the propagation of a necking region along the bar. The colourmap represents the damage intensity, red being higher damage. Propagation of a damage wave in the central part of the specimen was observed in the experimental data in [36] (see fig. S5 therein). (Online version in colour.)

and the stiffness increase at large strain. The green and orange dashed curves are the elastic stresses of each of the two terms in the Ogden model (3.6) with the parameters $\{\mu_1, \alpha_1, \mu_2, \alpha_2\}$ in table 2; at each material point, the elastic stress is the superposition of the responses of two nonlinear springs, one with $\{\mu_1, \alpha_1\} = \{4.6 \, \text{MPa}, 1.2\}$, which controls the response at low strains (dashed orange curve), and the other with $\{\mu_2, \alpha_2\} = \{0.012 \, \text{MPa}, 5.5\}$, which is activated at high strain and is responsible for the strain-hardening seen in the experiments (dashed green curve). In this sense, the model resembles the microscopic model proposed in [57], where a two-phase material model was considered. The insets in figure 10 show the damage field obtained from the numerical simulations at different levels of strain. At the position designated a in figure 10, the sudden appearance of a localized damage produces the drop in stress seen in the experiments, which corresponds to the occurrence of a necked region in the central part of the specimen, as shown in figure 11 (see also fig. S5 in [36]). The corresponding strain level $\varepsilon = 1.4$ is used to calibrate the value of the parameter λ_o. At increasing levels of strain, the necking enlarges with a constant maximum value up to the stretch at which it fills the whole specimen (region b in the figure). Thereafter (in region c) the damage value starts increasing, and at $\varepsilon = 4.55$ it was $d = 0.33$. The hardening behaviour is achieved in the model by taking the absolute value of a_3 to be large enough ($a_3 = -4.73$ in this case).

In order to highlight the capability of the model to describe the unloading process as well, unloading curves at different strain levels are shown in figure 10. The unloading branches follow paths with lower tangent stiffnesses due to the occurrence of damage, as also seen in the experimental data in [36]; as expected, no residual strains are observed at the complete unloading of the specimen. During the subsequent loading path, the curve perfectly follows the branch with lower stiffness up to the stress level at which damage starts increasing again. At high strain levels, this additional reduction of stress is compensated for by the elastic energy, which produces the stiffness increase seen at $\varepsilon > 300\%$, corresponding to the experimental situation of the elastomer network being completely unfolded.

The final numerical benchmark of the model corresponds to the deformation of a double-notch tension specimen that is normally used to estimate the critical fracture energy (see for instance [26,40]). The dimensions of the specimen, boundary conditions and mesh for this configuration are displayed in figure 12a and correspond to the experiments carried out in [56], with different lengths of the notch as shown in the insets (the same data were used as a benchmark problem in [23,33]). The constitutive parameters used in the simulation are those in table 3 with the elastic energy ϕ_A and fracture parameters $a_1 = 1.03$, $a_2 = 32.13$ and $a_3 = -0.81$. These parameters are in agreement with those reported in [23] to fit the same experimental data. Figure 12b shows the stress–strain curves, displaying the typical brittle response expected from elastomers in this
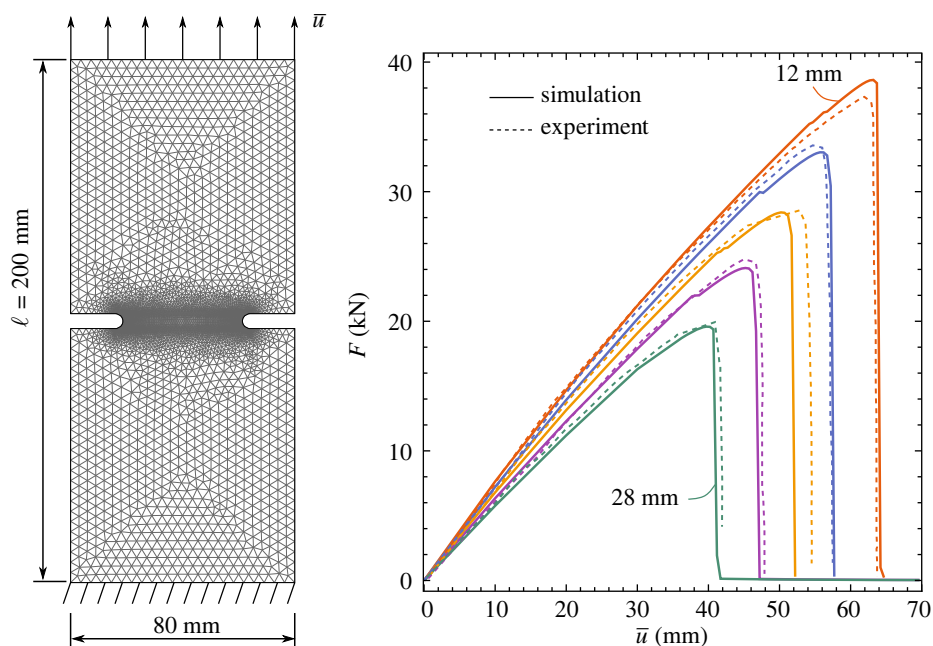
Figure 12. Geometry, mesh and boundary conditions of the double-notch tension specimen (left). Comparison of force–displacement curves with the constitutive parameters in table 3 and different notch semi-lengths {12, 26, 20, 24, 28} mm from Hocine *et al.* [56]. (Online version in colour.)

Table 3. Constitutive parameters used for the fitting of the experimental data in figure 12.

elastic				
$\mu_1 = 0.23$ MPa	$\alpha_1 = 2$			
fracture				
$\ell_f = 3.14$ mm,	$G_c = 3.15$ MPa mm,	$\lambda_o = 4.4$,	$\hat{k}_o = -9.53$ MPa mm,	$a_3 = -0.81$

type of test. The numerical results show a very narrow cohesive region in which the damage rapidly propagates between the notches up to the point at which it occupies the entire width and immediately jumps to 1, leading to catastrophic failure of the specimen.

The corresponding deformed configurations are shown in figure 13 at different levels of the overall strain. At $\bar{u} = 63.005$ mm the specimen is completely broken and, in fact, the material in the central part of the specimen is completely removed from the figure, having reached a value of d close to 1, with the lateral parts being almost unloaded.

5. Conclusion

We have presented a phenomenological phase-field model for the cohesive failure of elastomers at large strain. The elastic response of the model is described using an Ogden-like strain energy density, which has the advantage of accurately matching the quasi-static response of many materials up to significant strains. Fracture was incorporated by complementing the Ogden formulation with a phase-field variable, whose evolution was derived in a consistent thermodynamic framework by invoking the three principles of damage irreversibility, stability conditions and energy balance.
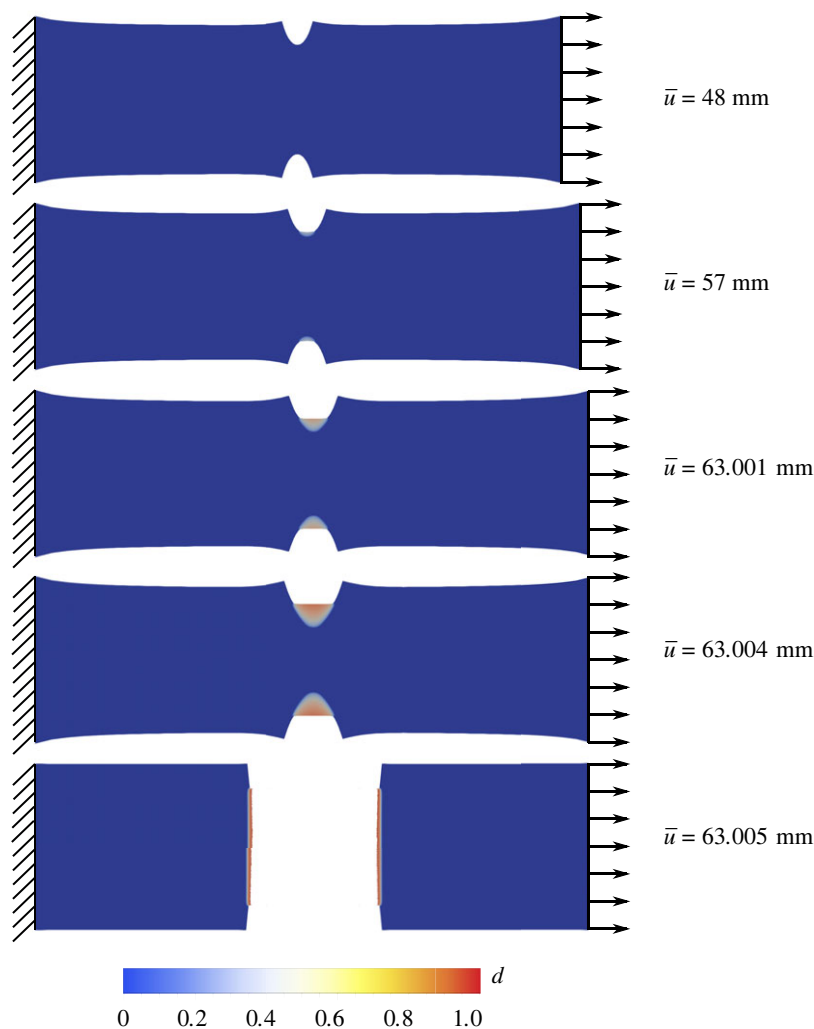
Figure 13. Deformed configuration of the double-notch tension specimen used for the numerical experiment in figure 12 with notch semi-length 12 mm. The colourmap represents the intensity of the damage field; at the final step, regions where $d \geq 0.99$ were removed from the plot. (Online version in colour.)

The fracture energy was defined according to a recent proposal in [17] in terms of five constitutive parameters: the energy release rate G_c, the internal length ℓ_f, which represents the size of the fracture process zone, and three coefficients a_1, a_2 and a_3 that define the energetic degradation function responsible for the stiffness decrease induced by damage. Analytical and numerical results were used to establish the connection between the shapes of the damage energy, degradation function and damage evolution modes. In particular, a_1 is related to the stretch at the damage onset in a one-dimensional test, a_2 depends on the slope of the cohesive curve, which is normally considered a material property, and, finally, a_3 influences the damage evolution at late stages. By properly tuning these constitutive parameters, the model is capable of matching a variety of fracture modes including brittle and pseudo-ductile failures, whereas most existing phase-field models at large strain (see e.g. [26]) can only describe brittle fracture. The application to double-network elastomers and conventional rubber compounds is discussed in the paper with reference to the experiments in [36,56]. The model was able to accurately capture the main features of the fracture process, such as the necking propagation and hardening stage at large strains for double-network elastomers, and brittle failure modes for conventional rubber compounds.

Compared with other approaches in the literature (such as [58]), the model does not use any information on the material microstructure, so it is suitable for a large class of materials including biological tissues.

The derivations were carried out by enforcing the plane stress condition and perfect incompressibility of the matrix. However, experimental evidence shows that fracture may occur due to the coalescence of voids and subsequent propagation of the defects, which may lead to a reduction of the apparent bulk modulus. Therefore, extensions of the model include the possibility of degrading with the phase-field variable both volumetric and isochoric parts of the energy. In addition, since viscous effects may become significant during the propagation of fractures, the incorporation of viscoelastic effects would be of paramount importance to correctly describe the dynamic evolution of fracture in elastomeric compounds.

Appendix A. Damage evolution regimes

An equation similar to (3.24) was already studied in [50] for a small-strain model (see eqn (31) therein). The solution strategy exploited there can be equally applied to the large-strain analysis carried out in this paper. In particular, the following steps allow us to calculate the unknown rates $\{\dot{u}_o, \dot{d}_o\}$: (i) first $\dot{d}_o$ is determined in terms of $\dot{S}_o$ by solving (3.24); (ii) then $\dot{S}_o$ is determined by evaluating the mean value, i.e. $\langle\cdot\rangle = (1/\ell)\int_0^\ell \cdot \, dx$, of both the sides of equation (3.20)$_2$, giving

$$\dot{S}_o = \omega_o'\phi_o'\langle\dot{d}_o\rangle + \phi_o''\dot{\varepsilon}_o, \tag{A 1}$$

where we have made use of the fact that $\dot{S}_o$ is constant along the bar and $\langle\dot{\lambda}_o\rangle = \dot{\varepsilon}_o$ by the boundary condition (3.10); (iii) finally, u is determined by integration of (3.20)$_2$ expressed in terms of $\dot{\lambda}_o = \dot{u}_o'$. Different solutions are found depending on the sign of j and on the ratio between the length ℓ and the internal lengths ℓ_i and ℓ_s, and their analytical expressions are presented in the following.

(a) For $j \geq 0$, the solution obtained by applying the procedure (i)–(iii) is

$$\dot{d}_o(x) = -\frac{\omega_o'\phi_o'}{j(1 + \langle g\rangle\ell_s/\ell_i)}\dot{\varepsilon}_o g(x) \quad \text{and} \quad \dot{S}_o = \frac{\phi''}{1 + \langle g\rangle\ell_s/\ell_i}\dot{\varepsilon}_o, \tag{A 2}$$

with

$$g(x) = 1 - \frac{\cosh(\pi(\ell - 2x)/\ell_i)}{\cosh(\pi\ell/\ell_i)} \quad \text{and} \quad \langle g\rangle = 1 - \frac{\ell_i}{\pi\ell}\tanh\left(\frac{\pi\ell}{\ell_i}\right). \tag{A 3}$$

Damage evolution is *full-size* in a regime of *stress-hardening*.

(b) For $j < 0$ and $\ell_i \geq \ell$, the solution is

$$\dot{d}_o(x) = -\frac{\omega'\phi'}{j(1 - \langle g\rangle\ell_s/\ell_i)}\dot{\varepsilon}_o g(x) \quad \text{and} \quad \dot{S}_o = \frac{\omega\phi_o''}{1 - \langle g\rangle\ell_s/\ell_i}\dot{\varepsilon}_o, \tag{A 4}$$

with

$$g(x) = 1 - \frac{\cos(\pi(\ell - 2x)/\ell_i)}{\cos(\pi\ell/\ell_i)} \quad \text{and} \quad \langle g\rangle = 1 - \frac{\ell_i}{\pi\ell}\tan\left(\frac{\pi\ell}{\ell_i}\right). \tag{A 5}$$

The solution $\dot{d}_o$ is *full-size* and two evolution regimes are obtained:

(1) (b.1)if $\ell_i > 2\ell$, the regime is *stress-hardening*, since $\langle g \rangle < 0$;
(2) (b.2)if $\ell < \ell_i \leq 2\ell$, the regime is *stress-softening*, as $\langle g \rangle > 0$. In this case, the condition

$$\langle g \rangle \geq \frac{\ell_i}{\ell_s} \tag{A 6}$$

must be satisfied to have $\dot{d}_o \geq 0$ everywhere.

(c) For $j < 0$ and $\ell_i < \ell$, the solution has the expression (A 4), with

$$g(x) = \begin{cases} 1 - \cos\left(\frac{2\pi x}{\ell_i}\right) & \text{if } 0 < x < \ell_i, \\ 0 & \text{if } x \geq \ell_i, \end{cases} \quad \text{and} \quad \langle g \rangle = \frac{\ell_i}{\ell}, \tag{A 7}$$

and so is localized in a portion of length ℓ_i (*localized solution*), and the evolution regime is *stress-softening*. Even in this case, the inequality

$$\ell \leq \ell_s \tag{A 8}$$

has to be fulfilled to have $\dot{d}_o \geq 0$.

It can be proved that inequalities (A 6) and (A 8) are necessary conditions for stability of the evolution problem (see [50]); indeed, they guarantee non-negativity of the second variation of the functional (3.12). If the stability conditions are not satisfied, the bar fails catastrophically at the time instant t_o, experiencing brittle fracture.

References

1. Ogden RW. 1972 Large deformation isotropic elasticity: on the correlation of theory and experiment for compressible rubberlike solids. *Proc. R. Soc. A* **328**, 567–583. (doi:10.1098/rspa.1972.0096)
2. Ogden RW. 1972 Large deformation isotropic elasticity—on the correlation of theory and experiment for incompressible rubberlike solids. *Proc. R. Soc. A* **326**, 565–584. (doi:10.1098/rspa.1972.0026)
3. Simo JC, Taylor RL. 1991 Quasi-incompressible finite elasticity in principal stretches. Continuum basis and numerical algorithms. *Comput. Methods Appl. Mech. Eng.* **85**, 273–310. (doi:10.1016/0045-7825(91)90100-K)
4. Yeoh OH. 1997 On the Ogden strain-energy function. *Rubber Chem. Technol.* **70**, 175–182. (doi:10.5254/1.3538422)
5. Saccomandi G, Ogden RW (eds.) 2004 *Mechanics and thermomechanics of rubberlike solids*, vol. 452 of CISM Courses and Lectures. Vienna, Austria: Springer.
6. Destrade M, Saccomandi G, Sgura I. 2017 Methodical fitting for mathematical models of rubber-like materials. *Proc. R. Soc. A* **473**, 20160811. (doi:10.1098/rspa.2016.0811)
7. Agostiniani V, DeSimone A. 2012 Ogden-type energies for nematic elastomers. *Int. J. Non-Linear Mech.* **47**, 402–412. (doi:10.1016/j.ijnonlinmec.2011.10.001)
8. Goriely A, Mihai LA. 2021 Liquid crystal elastomers wrinkling. *Nonlinearity* **34**, 5599–5629. (doi:10.1088/1361-6544/ac09c1)
9. Mills NJ, Fitzgerald C, Gilchrist A, Verdejo R. 2003 Polymer foams for personal protection: cushions, shoes and helmets. *Compos. Sci. Technol.* **63**, 2389–2400. (doi:10.1016/S0266-3538(03)00272-0)
10. Ciambella J, Bezazi A, Saccomandi G, Scarpa F. 2015 Nonlinear elasticity of auxetic open cell foams modeled as continuum solids. *J. Appl. Phys.* **117**, 184902. (doi:10.1063/1.4921101)
11. Moran R, Smith JH, García JJ. 2014 Fitted hyperelastic parameters for human brain tissue from reported tension, compression, and shear tests. *J. Biomech.* **47**, 3762–3766. (doi:10.1016/j.jbiomech.2014.09.030)
12. Macmanus DB, Pierrat B, Murphy JG, Gilchrist MD. 2016 Mechanical characterization of the P56 mouse brain under large-deformation dynamic indentation. *Sci. Rep.* **6**, 1–9. (doi:10.1038/srep21569)
13. Mihai LA, Budday S, Holzapfel GA, Kuhl E, Goriely A. 2017 A family of hyperelastic models for human brain tissue. *J. Mech. Phys. Solids* **106**, 60–79. (doi:10.1016/j.jmps.2017.05.015)

14. Saavedra Flores EI, Adhikari S, Friswell MI, Scarpa F. 2011 Hyperelastic finite element model for single wall carbon nanotubes in tension. *Comput. Mater. Sci.* **50**, 1083–1087. (doi:10.1016/j.commatsci.2010.11.005)

15. Valanis KC. 2022 The Valanis-Landel strain energy function elasticity of incompressible and compressible rubber-like materials. *Int. J. Solids Struct.* **238**, 111271. (doi:10.1016/j.ijsolstr.2021.111271)

16. Ogden RW, Saccomandi G, Sgura I. 2004 Fitting hyperelastic models to experimental data. *Comput. Mech.* **34**, 484–502. (doi:10.1007/s00466-004-0593-y)

17. Wu JY. 2017 A unified phase-field theory for the mechanics of damage and quasi-brittle failure. *J. Mech. Phys. Solids* **103**, 72–99. (doi:10.1016/j.jmps.2017.03.015)

18. Francfort GA, Marigo JJ. 1998 Revisiting brittle fracture as an energy minimization problem. *J. Mech. Phys. Solids* **46**, 1319–1342. (doi:10.1016/S0022-5096(98)00034-9)

19. Bourdin B, Francfort GA, Marigo JJ. 2000 Numerical experiments in revisited brittle fracture. *J. Mech. Phys. Solids* **48**, 797–826. (doi:10.1016/S0022-5096(99)00028-9)

20. Bourdin B, Francfort GA, Marigo JJ. 2008 The variational approach to fracture. *J. Elast.* **91**, 5–148. (doi:10.1007/s10659-007-9107-3)

21. Miehe C, Hofacker M, Welschinger F. 2010 A phase field model for rate-independent crack propagation: robust algorithmic implementation based on operator splits. *Comput. Methods Appl. Mech. Eng.* **199**, 2765–2778. (doi:10.1016/j.cma.2010.04.011)

22. Pham K, Amor H, Marigo JJ, Maurini C. 2011 Gradient damage models and their use to approximate brittle fracture. *Int. J. Damage Mech.* **20**, 618–652. (doi:10.1177/1056789510386852)

23. Miehe C, Schänzel LM. 2014 Phase field modeling of fracture in rubbery polymers. Part I: finite elasticity coupled with brittle failure. *J. Mech. Phys. Solids* **65**, 93–113. (doi:10.1016/j.jmps.2013.06.007)

24. Marigo JJ, Maurini C, Pham K. 2016 An overview of the modelling of fracture by gradient damage models. *Meccanica* **51**, 3107–3128. (doi:10.1007/s11012-016-0538-4)

25. Del Piero G, Lancioni G, March R. 2007 A variational model for fracture mechanics: numerical experiments. *J. Mech. Phys. Solids* **55**, 2513–2537. (doi:10.1016/j.jmps.2007.04.011)

26. Loew PJ, Peters B, Beex LA. 2019 Rate-dependent phase-field damage modeling of rubber and its experimental parameter identification. *J. Mech. Phys. Solids* **127**, 266–294. (doi:10.1016/j.jmps.2019.03.022)

27. Hesch C, Weinberg K. 2014 Thermodynamically consistent algorithms for a finite-deformation phase-field approach to fracture. *Int. J. Numer. Methods Eng.* **99**, 906–924. (doi:10.1002/nme.4709)

28. Henao D, Mora-Corral C, Xu X. 2016 A numerical study of void coalescence and fracture in nonlinear elasticity. *Comput. Methods Appl. Mech. Eng.* **303**, 163–184. (doi:10.1016/j.cma.2016.01.012)

29. Kumar A, Francfort GA, Lopez-Pamies O. 2018 Fracture and healing of elastomers: a phase-transition theory and numerical implementation. *J. Mech. Phys. Solids* **112**, 523–551. (doi:10.1016/j.jmps.2018.01.003)

30. Kumar A, Lopez-Pamies O. 2020 The phase-field approach to self-healable fracture of elastomers: a model accounting for fracture nucleation at large, with application to a class of conspicuous experiments. *Theor. Appl. Fract. Mech.* **107**, 102550. (doi:10.1016/j.tafmec.2020.102550)

31. Poulain X, Lefèvre V, Lopez-Pamies O, Ravi-Chandar K. 2017 Damage in elastomers: nucleation and growth of cavities, micro-cracks, and macro-cracks. *Int. J. Fract.* **205**, 1–21. (doi:10.1007/s10704-016-0176-9)

32. Poulain X, Lopez-Pamies O, Ravi-Chandar K. 2018 Damage in elastomers: healing of internally nucleated cavities and micro-cracks. *Soft Matter* **14**, 4633–4640. (doi:10.1039/C8SM00238J)

33. Talamini B, Mao Y, Anand L. 2018 Progressive damage and rupture in polymers. *J. Mech. Phys. Solids* **111**, 434–457. (doi:10.1016/j.jmps.2017.11.013)

34. Li B, Bouklas N. 2020 A variational phase-field model for brittle fracture in polydisperse elastomer networks. *Int. J. Solids Struct.* **182–183**, 193–204. (doi:10.1016/j.ijsolstr.2019.08.012)

35. Toulemonde PA, Diani J, Gilormini P, Desgardin N. 2016 On the account of a cohesive interface for modeling the behavior until break of highly filled elastomers. *Mech. Mater.* **93**, 124–133. (doi:10.1016/j.mechmat.2015.09.014)

36. Millereau P, Ducrot E, Clough JM, Wiseman ME, Brown HR, Sijbesma RP, Creton C. 2018 Mechanics of elastomeric molecular composites. *Proc. Natl Acad. Sci. USA* **115**, 9110–9115. (doi:10.1073/pnas.1807750115)

37. Zhao Z, Lei H, Chen HS, Zhang Q, Wang P, Lei M. 2021 A multiscale tensile failure model for double network elastomer composites. *Mech. Mater.* **163**, 104074. (doi:10.1016/j.mechmat.2021.104074)

38. Mueller H, Knauss W. 1971 Fracture energy and some mechanical properties of a polyurethane elastomer. *Trans. Soc. Rheol.* **15**, 217–233. (doi:10.1122/1.549209)

39. Amor H, Marigo JJ, Maurini C. 2009 Regularized formulation of the variational brittle fracture with unilateral contact: numerical experiments. *J. Mech. Phys. Solids* **57**, 1209–1229. (doi:10.1016/j.jmps.2009.04.011)

40. Miehe C, Welschinger F, Hofacker M. 2010 Thermodynamically consistent phase-field models of fracture: variational principles and multi-field FE implementations. *Int. J. Numer. Methods Eng.* **83**, 1273–1311. (doi:10.1002/nme.2861)

41. Freddi F, Royer-Carfagni G. 2010 Regularized variational theories of fracture: a unified approach. *J. Mech. Phys. Solids* **58**, 1154–1174. (doi:10.1016/j.jmps.2010.02.010)

42. Marigo JJ. 1989 Constitutive relations in plasticity, damage and fracture mechanics based on a work property. *Nucl. Eng. Des.* **114**, 249–272. (doi:10.1016/0029-5493(89)90105-2)

43. Lancioni G. 2015 Modeling the response of tensile steel bars by means of incremental energy minimization. *J. Elast.* **121**, 25–54. (doi:10.1007/s10659-015-9515-8)

44. Alessi R, Marigo J-J, Vidoli S. 2015 Gradient damage models coupled with plasticity: variational formulation and main properties. *Mech. Mater.* **80**, 351–367. (doi:10.1016/j.mechmat.2013.12.005)

45. Lancioni G, Alessi R. 2020 Modeling micro-cracking and failure in short fiber-reinforced composites. *J. Mech. Phys. Solids* **137**, 103854. (doi:10.1016/j.jmps.2019.103854)

46. Wu JY. 2018 Robust numerical implementation of non-standard phase-field damage models for failure in solids. *Comput. Methods Appl. Mech. Eng.* **340**, 767–797. (doi:10.1016/j.cma.2018.06.007)

47. Mielke A, Roubíček T. 2015 *Rate-independent systems: theory and application*. New York, NY: Springer.

48. Ogden RW. 2001 Pseudo-elasticity and stress softening. In *Nonlinear elasticity: theory and applications* (eds YB Fu, RW Ogden), pp. 491–522. Cambridge, UK: Cambridge University Press.

49. Farrell P, Maurini C. 2017 Linear and nonlinear solvers for variational phase-field models of brittle fracture. *Int. J. Numer. Methods Eng.* **109**, 648–667. (doi:10.1002/nme.5300)

50. Lancioni G, Corinaldesi V. 2018 Variational modelling of diffused and localized damage with applications to fiber-reinforced concretes. *Meccanica* **53**, 531–551. (doi:10.1007/s11012-017-0709-y)

51. Nonato Da Silva C, Ciambella J, Barros J, Costa I. 2019 Analytical bond model for general type of reinforcements of finite embedment length in cracked cement based materials. *Int. J. Solids Struct.* **167**, 36–47. (doi:10.1016/j.ijsolstr.2019.02.018)

52. Da Silva CN, Ciambella J, Barros J, dos Santos Valente T, Costa I. 2020 A multiscale model for optimizing the flexural capacity of FRC structural elements. *Compos. Part B: Eng.* **200**, 108325. (doi:10.1016/j.compositesb.2020.108325)

53. Wu JY, Nguyen VP. 2018 A length scale insensitive phase-field damage model for brittle fracture. *J. Mech. Phys. Solids* **119**, 20–42. (doi:10.1016/j.jmps.2018.06.006)

54. Yin T, Wu T, Liu J, Qu S, Yang W. 2021 Essential work of fracture of soft elastomers. *J. Mech. Phys. Solids* **156**, 104616. (doi:10.1016/j.jmps.2021.104616)

55. Logg A, Mardal K-A, Wells G, (eds.) 2012 *Automated solution of differential equations by the finite element method*, vol. 84 of Lecture Notes in Computational Science and Engineering. Berlin, Germany: Springer.

56. Hocine NA, Abdelaziz MN, Imad A. 2002 Fracture problems of rubbers: J-integral estimation based upon η factors and an investigation on the strain energy density distribution as a local criterion. *Int. J. Fract.* **117**, 1–23. (doi:10.1023/A:1020967429222)

57. De Tommasi D, Puglisi G, Saccomandi G. 2008 Localized versus diffuse damage in amorphous materials. *Phys. Rev. Lett.* **100**, 1–4. (doi:10.1103/PhysRevLett.100.085502)

58. Lavoie SR, Millereau P, Creton C, Long R, Tang T. 2019 A continuum model for progressive damage in tough multinetwork elastomers. *J. Mech. Phys. Solids* **125**, 523–549. (doi:10.1016/j.jmps.2019.01.001)